HHS Public Access

Author manuscript

Cell Metab. Author manuscript; available in PMC 2025 October 01.

Published in final edited form as:

Cell Metab. 2024 October 01; 36(10): 2207–2227.e9. doi:10.1016/j.cmet.2024.08.006.

m^{6}A mRNA methylation in brown fat regulates systemic insulin sensitivity via an inter-organ prostaglandin signaling axis independent of UCP1

Ling Xiao[1,11], **Dario F. De Jesus**[1,11], **Cheng-Wei Ju**[2,11], **Jiang Bo Wei**[2,10], **Jiang Hu**[1], **Ava DiStefano-Forti**[1], **Tadataka Tsuji**[3], **Cheryl Cero**[4], **Ville Männistö**[5], **Suvi M. Manninen**[6], **Siying Wei**[7], **Oluwaseun Ijaduola**[1], **Matthias Blüher**[8], **Aaron M. Cypess**[4], **Jussi Pihlajamäki**[6,9], **Yu-Hua Tseng**[3], **Chuan He**[2], **Rohit N. Kulkarni**[1,12,*]

[1]Section of Islet Cell and Regenerative Biology, Joslin Diabetes Center, Department of Medicine, BIDMC, Harvard Stem Cell Institute, Harvard Medical School, Boston, MA, USA

[2]Department of Chemistry, Howard Hughes Medical Institute, The University of Chicago, Chicago, IL, USA

[3]Section on Integrative Physiology and Metabolism, Joslin Diabetes Center, Department of Medicine, BIDMC, Harvard Medical School, Harvard Stem Cell Institute, Boston, MA, USA

[4]Diabetes, Endocrinology, and Obesity Branch, Intramural Research Program, National Institute of Diabetes and Digestive and Kidney Diseases (NIDDK), NIH, Bethesda, MD, USA

[5]Department of Medicine, University of Eastern Finland and Kuopio University Hospital, Kuopio, Finland

[6]Institute of Public Health and Clinical Nutrition, Faculty of Health Sciences, University of Eastern Finland, Kuopio, Finland

[*]Correspondence: rohit.kulkarni@joslin.harvard.edu.

AUTHOR CONTRIBUTIONS

L.X. and D.F.D.J. conceived the study, designed and performed experiments, analyzed the data, assembled figures, and wrote the manuscript. C.-W.J. performed RNA/m^{6}A-seq and m^{6}A LC-MS/MS experiments, as well as bioinformatics analysis. J.B.W. assisted with m^{6}A-seq and m^{6}A LC-MS/MS experiments. J.H. performed immunohistochemistry. A.D.-F. assisted with animal experiments. T.T. performed correlation analyses for human cohort 1 and assisted with AAV injection. C.C. provided RT-qPCR data of human BAT tissues. V.M. collected plasma and other clinical data of human cohort 2. S.M.M. collected plasma and other clinical data of human cohort 3. S.Y.W. generated *METTL14*-OE and control lentiviral vectors. O.I. assisted with animal experiments. M.B. provided human plasma samples for human cohort 1 and edited the manuscript. A.M.C. contributed to conceptual discussions and provided data related to human brown adipose tissues. J.P. was responsible for human cohorts 2 and 3 as PI and contributed to conceptual discussions. Y.-H.T. contributed to conceptual discussions, shared lipidomics data of human cohort 1, and provided immortalized human white/brown preadipocytes and protocols for culture and differentiation. C.H. contributed to conceptual discussions and designed the experiments for RNA-seq and m^{6}A-seq. R.N.K. conceived the study, designed the experiments, supervised the project, and wrote the manuscript. All the authors have reviewed, commented on, and edited the manuscript.

DECLARATION OF INTERESTS

R.N.K. is on the scientific advisory boards of Novo Nordisk, Biomea, Inversago, and REDD. C.H. is a scientific founder and a member of the scientific advisory board of Accent Therapeutics. M.B. received honoraria as a consultant and speaker from Amgen, AstraZeneca, Bayer, Boehringer Ingelheim, Lilly, Novo Nordisk, Novartis, Pfizer, and Sanofi.

DECLARATION OF GENERATIVE AI AND AI-ASSOCIATED TECHNOLOGIES IN THE WRITING PROCESS

During the preparation of this work the authors used ChatGPT3.5 in order to improve language and readability. After using this tool/service, the authors reviewed and edited the content as needed and take full responsibility for the content of the publication.

SUPPLEMENTAL INFORMATION

Supplemental information can be found online at https://doi.org/10.1016/j.cmet.2024.08.006.

[7]Section of Islet Cell and Regenerative Biology, and CRISPR Screen Core Laboratory, Joslin Diabetes Center, Department of Medicine, BIDMC, Harvard Medical School, Boston, MA, USA

[8]Helmholtz Institute for Metabolic, Obesity and Vascular Research (HI-MAG), University of Leipzig and University Hospital Leipzig, Leipzig, Germany

[9]Endocrinology and Clinical Nutrition, Kuopio University Hospital, Kuopio, Finland

[10]Present address: Department of Chemistry and Department of Biological Sciences, National University of Singapore, Singapore, Singapore

[11]These authors contributed equally

[12]Lead contact

SUMMARY

Brown adipose tissue (BAT) regulates systemic metabolism by releasing signaling lipids. N^6-methyladenosine (m^6A) is the most prevalent and abundant post-transcriptional mRNA modification and has been reported to regulate BAT adipogenesis and energy expenditure. Here, we demonstrate that the absence of m^6A methyltransferase-like 14 (METTL14) modifies the BAT secretome to improve systemic insulin sensitivity independent of UCP1. Using lipidomics, we identify prostaglandin E2 (PGE2) and prostaglandin F2a (PGF2a) as BAT-secreted insulin sensitizers. PGE2 and PGF2a inversely correlate with insulin sensitivity in humans and protect mice from high-fat-diet-induced insulin resistance by suppressing specific AKT phosphatases. Mechanistically, METTL14-mediated m^6A promotes the decay of *PTGES2* and *CBR1*, the genes encoding PGE2 and PGF2a biosynthesis enzymes, in brown adipocytes via YTHDF2/3. Consistently, BAT-specific knockdown of *Ptges2* or *Cbr1* reverses the insulin-sensitizing effects in $M14^{KO}$ mice. Overall, these findings reveal a novel biological mechanism through which m^6A-dependent regulation of the BAT secretome regulates systemic insulin sensitivity.

In brief

m^6A mRNA modification has been reported to play pivotal roles in various metabolic tissues. Here, Xiao et al. reveal a novel mechanism whereby m^6A controls whole-body insulin sensitivity via regulating prostaglandin biosynthesis in brown adipocytes.

Graphical Abstract

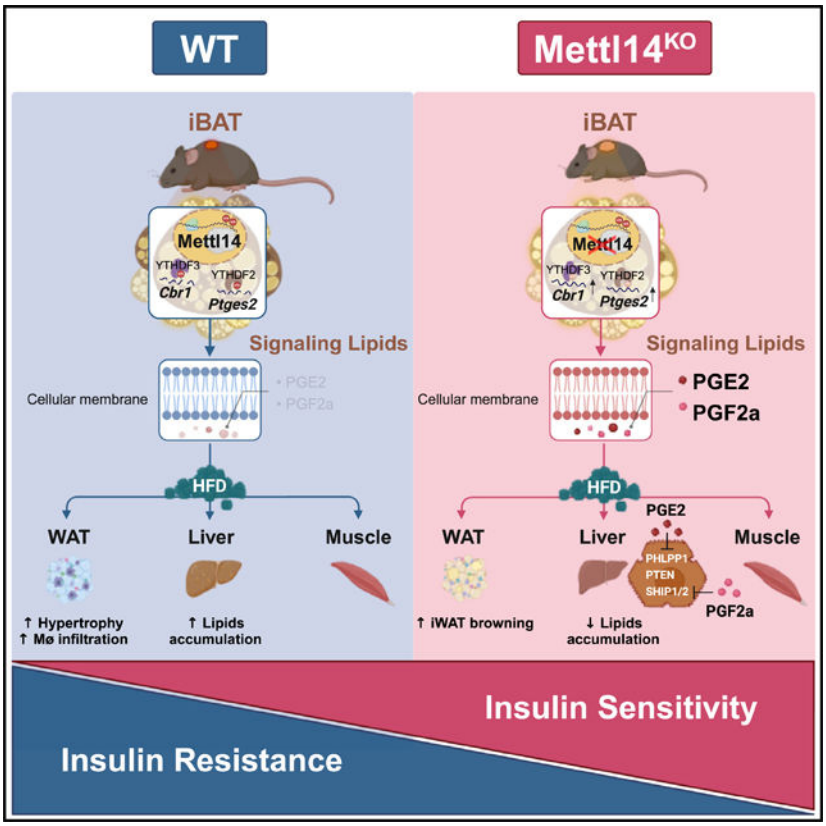

INTRODUCTION

Brown adipose tissue (BAT) has emerged as a potential target for the treatment and prevention of human obesity and related metabolic disorders secondary to its thermogenic function mediated by uncoupling protein 1 (UCP1). In humans, BAT-mediated energy expenditure under cold exposure contributes to body fat reduction.[1,2] BAT has also been reported to promote cardiometabolic health, especially in individuals who are overweight or obese.[3] Although BAT has been traditionally recognized for its thermogenic capacity upon cold stimulation, it can also provide metabolic benefits by its ability to assist in the utilization of nutrients (e.g., glucose, fatty acids, branched-chain amino acids) during energy dissipation and via actions of secreted factors.[4]

Notably, BAT has been reported to exert positive effects on systemic metabolism via secreted factors that include peptides, proteins, lipids, or microRNAs.[4,5] In particular, a class of lipids known as “BAT lipokines” has attracted attention in recent years.[4,5] The term “lipokine” was first defined as an adipose tissue-secreted lipid hormone linking to systemic metabolic processes, including the regulation of insulin sensitivity, glucose tolerance, and inflammation.[6] For example, 12,13-diHOME, induced by cold and exercise, enhances fatty acid transport into BAT, reducing circulating triglycerides,[7] and promotes fatty acid uptake in skeletal muscle.[8] 12-HEPE, another cold-induced BAT lipokine, stimulates glucose uptake into BAT and muscle.[9] Additionally, BAT-secreted lipids such as maresin 2 mediate anti-inflammatory BAT-liver crosstalk.[10]

N^6-methyladenosine (m^6A) is the most prevalent, abundant, and conserved internal post-transcriptional modification in eukaryotic mRNAs.[11] The modification is primarily orchestrated by the writer complex, which consists of methyltransferase-like 14 (METTL14), methyltransferase-like 3 (METTL3), and Wilms' tumor 1-associated protein (WTAP),[12] among other proteins. Removal of m^6A is performed by demethylases such as fat mass and obesity-associated protein (FTO) or alkB homolog 5 (ALKBH5). The effects of the m^6A modification on mRNA metabolism depend largely on the recognition by different m^6A reader proteins to allow for regulation of mRNA stability, translation, splicing, and/or export. For instance, recognition of m^6A by YTH N(6)-methyladenosine RNA binding protein 2 (YTHDF2) or YTH N(6)-methyladenosine RNA binding protein 3 (YTHDF3) controls mRNA decay of the targeted mRNAs.[11,13]

While recent studies have implicated m^6A modification in diverse physiological processes including the regulation of human β cell biology[14–16] and in brown/beige adipogenesis and/or thermogenesis,[17–19] its significance in modifying the BAT secretome to regulate systemic insulin sensitivity remains unexplored.

In the present study, we propose that METTL14 regulates BAT secretory function by a unique mechanism that is independent of UCP1 to regulate systemic insulin sensitivity. BAT-specific *Mettl14* knockout ($M14^{KO}$) mice displayed improved insulin sensitivity and glucose tolerance independent of body weight, sex, or canonical BAT thermogenesis. Untargeted lipidomics profiling of mouse BAT and human brown adipocytes (hBATs) identified an upregulation of prostaglandin E2 (PGE2), prostaglandin D2 (PGD2), prostaglandin F2 alpha (PGF2a), and 13,14-dh-15-keto-PGE2 secondary to METTL14 deficiency. PGE2 and PGF2a improve systemic insulin sensitivity by suppressing AKT phosphatases in key peripheral metabolic tissues. Mechanistically, METTL14 deficiency in BAT prevents the decay of *PTGES2* and *CBR1* transcripts encoding prostaglandin biosynthesis enzymes to enable an increase in their protein levels. Downregulation of *Ptges2* or *Cbr1* gene in $M14^{KO}$-interscapular BAT (iBAT) reverses the insulin-sensitizing phenotype.

Taken together, these results argue for a novel mechanism coupling m^6A methylation with the BAT secretome to regulate systemic insulin sensitivity, independent of canonical BAT thermogenesis.

RESULTS

Mettl14 deficiency in BAT improves systemic insulin sensitivity and glucose tolerance independent of UCP1-mediated thermogenesis in mice

First, to determine whether the expression of m^6A writers is altered in obesity and insulin-resistant states, we performed RT-qPCR analyses in human BAT biopsies obtained from non-obese (body mass index [BMI] < 30) or obese (BMI ≥ 30) humans. Gene expression of *METTL14*, but not *METTL3* or *WTAP*, was dramatically upregulated in BAT from individuals who are obese compared with those who are non-obese (Figure 1A). To investigate the involvement of BAT m^6A in systemic insulin sensitivity, we examined mouse models of systemic insulin resistance. We analyzed the expression levels of m^6A writers METTL14, METTL3, and WTAP in the iBAT samples of a genetic hyperphagic mouse

model of insulin resistance,[20] namely, the leptin receptor-deficient *db/db* mouse. *db/db* mice exhibited higher Mettl14 at both mRNA (Figure 1B) and protein (Figures 1C and S1A) levels, compared with controls. Next, to distinguish insulin sensitivity from obesity, we took advantage of the liver-specific insulin receptor knockout (LIRKO) mouse model, which exhibits severe insulin resistance in the absence of obesity.[21] *Mettl14* gene and protein expression levels in iBAT were upregulated in the LIRKOs, compared with littermate controls (Figures 1D, 1E, and S1B). These findings suggest a potential role for METTL14 in modulating BAT function to regulate systemic insulin sensitivity and metabolic homeostasis.

To directly interrogate the role of METTL14, we generated BAT-specific $M14^{KO}$ mice by crossing *Mettl14*-floxed ($M14^{fl/fl}$) animals[14] with *Ucp1*-cre mice.[22] We verified specific depletion of *Mettl14* in iBAT and did not observe significant alterations in protein abundance or gene expression in other metabolic tissues such as inguinal white adipose tissue (iWAT), epididymal white adipose tissue (eWAT), liver, or muscle (Figures S1C–S1F), or in non-metabolic tissues including kidney, thymus, hypothalamus, or adrenal gland (data not shown), of $M14^{fl/fl}$-UCP1-cre (referred to as $M14^{KO}$) mice, compared with controls ($M14^{fl/fl}$). $M14^{KO}$ and control mice were born in a normal Mendelian ratio and exhibited no developmental defects (data not shown).

To explore the role of METTL14 under physiological conditions, we first placed both female and male mice on a chow diet (CD). Deficiency of *Mettl14* did not show significant differences in body weights between the groups fed with CD (Figure 1F). However, both sexes of $M14^{KO}$ mice showed improved insulin sensitivity and glucose tolerance (Figures 1G–1J).

To further examine the ability of $M14^{KO}$ mice to handle insulin resistance, we fed mice with a high-fat diet (HFD) (60% fat) and compared them with mice fed a low-fat diet (LFD) (10% fat). $M14^{KO}$ mice on HFD were smaller in body size (Figure S1G) and exhibited increased iBAT but decreased iWAT, eWAT, and liver mass (Figure S1H). Consistently, hematoxylin and eosin (H&E) staining revealed larger brown adipocytes (Figure S1I) while smaller adipocytes were detected in iWAT (Figure S1J) and eWAT (Figure S1K) in HFD-fed $M14^{KO}$ mice. Interestingly, although HFD increased the brown adipocyte size in controls, it did not significantly affect that of $M14^{KO}$ mice (Figure S1I), suggesting increased adipocyte numbers in the mutants. Adipocytes in the iWAT (Figure S1J) and eWAT (Figure S1K) from HFD-$M14^{KO}$ mice were visually smaller, compared with controls. Surprisingly, immunohistochemical (IHC) staining revealed lower UCP1 abundance in $M14^{KO}$-iBAT (Figure S1I). Conversely, UCP1-positive cells were present in the iWAT of LFD-$M14^{KO}$ mice (Figure S1J), suggesting the browning of WAT. In contrast to controls, $M14^{KO}$ mice were protected from HFD-induced macrophage infiltration, as indicated by F8/ 40 IHC staining in eWAT (Figure S1K), and hepatic steatosis (Figure S1L).

As expected, control female mice fed HFD presented increased body weights, elevated fasting insulin levels, and insulin resistance as measured by the homeostatic model assessment of insulin resistance (HOMA-IR), compared with control female mice fed an LFD (Figures 1K–1P). In contrast, female $M14^{KO}$ mice were protected against HFD-induced insulin resistance and presented lower fasting insulin levels and improved HOMA-

IR, compared with controls on HFD (Figures 1K–1N). Thus, female M14^{KO} mice presented improved insulin sensitivity and glucose tolerance profiles independent of the diet, compared with controls (Figures 1O and 1P). Similar changes were observed in males (Figures 1Q–1V).

Serum adiponectin levels were elevated in M14^{KO} female mice, compared with littermate controls, on the LFD (Figure S1M) but were similar between males (Figure S1O). Circulating leptin levels were similar between groups on LFD in both sexes (Figures S1N and S1P, left); however, the HFD-induced elevation in leptin in controls in both sexes was blunted in the M14^{KO} mice (Figures S1N and S1P, right). Overall, these data suggest that *Mettl14* ablation in BAT improves insulin sensitivity and glucose tolerance independent of body weight changes or diet.

Finally, we investigated the role of UCP1 in the observed phenotypes of M14^{KO} mice. The reduced UCP1 protein abundance in M14^{KO}-iBAT (Figures S1I, S1Q, and S1R) led us to hypothesize that the enhanced insulin sensitivity and glucose tolerance in M14^{KO} mice occur independently of the canonical UCP1-mediated thermogenesis in BAT. To explore this hypothesis, two independent cohorts of mice were subjected to either cold (5°C) or thermoneutral conditions (30°C) for 7 days to activate or deactivate UCP1 activity, respectively. Despite these conditions, M14^{KO} mice consistently exhibited improved insulin sensitivity and glucose tolerance (Figures 1W–1Z). Additionally, although M14^{KO} mice displayed PGC1α and UCP1 protein expression in iWAT (Figures S1S and S1T) and enhanced cold tolerance (Figure S1U), their energy expenditure (Figure S1V), oxygen consumption (Figure S1W), and carbon dioxide production (Figure S1X) were comparable to those of control mice. These results confirm our hypothesis that the enhanced insulin sensitivity and glucose tolerance phenotypes are indeed independent of the classical BAT thermogenesis.

Taken together, these results indicate that *METTL14* deficiency in BAT improves whole-body insulin sensitivity, independent of body weight reduction and canonical BAT thermogenesis.

M14^{KO}-BAT-secreted factors enhance insulin sensitivity in peripheral metabolic tissues in mice and primary metabolic cells in humans

The improved insulin sensitivity following ablation of *Mettl14* in iBAT, which was independent of gender, body weight reduction, and UCP1-mediated thermogenesis, prompted us to examine the tissue-specific insulin-sensitizing effects using *in vivo* insulin stimulation experiments. To this end, we performed *in vivo vena cava* insulin infusion in the various groups, followed by the harvesting of metabolic tissues post-insulin stimulation for analyses (Figure 2A). M14^{KO} mice displayed a dramatically higher hepatic serine 473 phosphorylation of protein kinase B (pAKT$_{s473}$), compared with controls, independent of diet or insulin-stimulated phosphorylation of insulin or IGF1 receptors (IRβ/IGF1Rβ) (Figures 2B and 2C).

Additionally, when fed an LFD, M14^{KO} mice exhibited elevated pAKT$_{s473}$ in both their eWAT (Figures 2D and 2E) and iWAT (Figures 2F and 2G), compared with controls. The

typical decrease in pIRβ/IGF1Rβ and $pAKT_{s473}$ that is observed in response to HFD in controls was not detected in eWAT (Figures 2D and 2E) or iWAT (Figures 2F and 2G) from $M14^{KO}$ mice.

While $M14^{KO}$ mice fed with LFD showed reduced pIRβ/IGF1Rβ in muscle, they demonstrated increased $pAKT_{s473}$ activation, compared with control mice on the same diet (Figures 2H and 2I). When challenged with HFD, $M14^{KO}$ mice exhibited higher levels of both pIRβ/IGF1Rβ and $pAKT_{s473}$ in their muscle, compared with control mice (Figures 2H and 2I).

Of note, no significant difference in pIRβ/IGF1Rβ and $pAKT_{s473}$ levels was observed in iBAT between control and $M14^{KO}$ mice on LFD (Figures S2A and S2B). While an increase in pIRβ/IGF1Rβ was observed in $M14^{KO}$-iBAT, compared with control-iBAT in response to HFD, there were no differences in $pAKT_{s473}$ levels between control- and $M14^{KO}$-iBAT (Figures S2A and S2B). These findings suggest that the lack of *Mettl14* in iBAT leads to increased insulin-stimulated responses primarily in the peripheral metabolic tissues, underscoring inter-organ communication in the $M14^{KO}$ mouse model.

Our data thus far suggested that secretory factor(s) released by $M14^{KO}$-BAT can enhance insulin sensitivity in distant metabolic organs, thereby enhancing systemic insulin sensitivity. To test this further, we generated three stable $M14^{KO}$ human brown preadipocytes (sgM14#1-, sgM14#2-, and sgM14#3-hBAT) by using single-guide RNA particles; single-guide non-targeting control (sgNTC) RNA transfected hBAT cells were also generated as controls (Figure 2J). METTL14 knockout in differentiated hBAT cells was confirmed by western blot analysis (Figure S2C). Notably, *METTL14* depletion in hBAT cells resulted in an improved differentiation capacity as determined by oil red O staining (Figure S2D).

Next, we explored the relevance of METTL14 in regulating secretory function in hBAT cells. To mimic the *in vivo* setting, we performed co-culture experiments by treating differentiated human white adipocytes (hWATs), primary human hepatocytes (hHepatocytes), or differentiated primary human myotubes (hMyotubes) with serum-free conditioned media from differentiated sgNTC- or sgM14-hBAT cells, followed by analyses of the insulin-stimulated signaling of the recipient cells (Figure 2J). Consistent with our *in vivo* data, the conditioned media from sgM14-hBAT increased $pAKT_{s473}$ levels in differentiated hWAT cells in comparison to that from sgNTC-hBAT (Figures 2K and 2L). Consistently, conditioned media from sgM14-hBAT boosted $pAKT_{s473}$ levels in hHepatocytes (Figures 2M and 2N) or hMyotubes (Figures 2O and 2P) in response to insulin, when compared with cells treated with conditioned media from sgNTC-hBAT. Collectively, both *in vivo* and *in vitro* data strongly support our hypothesis that METTL14 ablation in BAT promotes the systemic release of brown adipocyte “factors” that promote intracellular insulin sensitization in distant metabolic tissues.

Identification of PGE2 and PGF2a as major $M14^{KO}$-BAT-secreted insulin sensitizers

We next sought to identify the putative factors secreted by brown adipocytes from $M14^{KO}$ mice. The ability of denatured hBAT-conditioned media to induce an improvement in $pAKT_{s473}$ levels, similar to the non-denatured conditioned media in hWAT cells (Figure

S3A), allowed us to conclude that one or more factors released by the $M14^{KO}$-brown adipocytes were likely signaling lipids.

To specifically identify the lipids secreted by the $M14^{KO}$-brown adipocytes, we applied comprehensive untargeted liquid chromatography-tandem mass spectrometry (LC-MS/MS) signaling lipidomics to five sets of samples. First, we collected plasma from overnight-fasted mice to evaluate circulating lipids (Figure 3A, left). In addition, we performed an *ex vivo* culture of the iBAT explant and collected conditioned Krebs solution (CKS) as well as the iBAT tissue after a 2-h culture at 37°C for examining BAT-secreted lipids[7] (Figure 3A, left). Furthermore, considering iBAT is a heterogeneous tissue, we employed stable $M14^{KO}$-hBAT cells to ensure the secreted factors are specifically from brown adipocytes. Thus, we differentiated hBAT cells and collected conditioned culture media as well as cell pellets (Figure 3A, right).

Multivariate statistical models of the lipid profiling data were used to identify common lipids enriched in the five $M14^{KO}$ sample types (Figures S3B–S3F). Comparative analyses of the individual signaling lipids between control and $M14^{KO}$ samples (Figures 3B, S3G, and S3H) led to the identification of 66 species that showed overlap among iBAT, iBAT-CKS, and hBAT conditioned media (Figure 3C). Besides, when intersecting iBAT, CKS, and plasma samples, 75 lipids were commonly expressed among the three sets (Figure S3I). We noted that 73 lipids overlapped between conditioned hBAT media and hBAT cells (Figure S3J), while 82 lipids overlapped among conditioned hBAT media, CKS, and plasma (Figure S3K). Importantly, four lipid species that belonged to the prostanoid family, namely, PGE2, PGD2, PGF2a, and 13,14-dihydro-15-keto-PGE2 (13,14-dh-15-keto-PGE2), were consistently significantly ($p < 0.05$) increased in a majority of the samples ($M14^{KO}$-iBAT, $M14^{KO}$-iBAT-CKS, and sgM14-hBAT-conditioned media) (Figure 3C). Next, we validated this observation by confirming the upregulation of PGE2 and PGF2a in independent sets of mouse plasma, iBAT-CKS, and hBAT culture media, using enzyme-linked immunosorbent assays (ELISAs). Consistently, the absolute concentration of these two lipids was higher in the $M14^{KO}$ samples compared with controls (Figures 3D and 3E). Interestingly, due to the short half-life of both PGs, their concentrations were lower in the plasma than in the cultured media. These data suggest that PGE2, PGD2, PGF2a, and 13,14-dh-15-keto-PGE2 are potential lipokines secreted by $M14^{KO}$-BAT.

To directly validate whether the candidate prostaglandins are responsible for the observed improvement in insulin sensitivity in peripheral metabolic cells, we performed a series of independent dose-response studies in a human liver cell line (HepG2) (Figure S4A), a differentiated mouse skeletal muscle cell line (C2C12) (Figure S4B), differentiated hWAT cells (Figure S4C), or differentiated hBAT cells (Figure S4D). Briefly, cells were treated with physiological (10 and 100 nM) or supraphysiological concentrations (1,000 nM) of PGE2, PGD2, PGF2a, or 13,14-dh-15-keto-PGE2 overnight. Cells were then washed and stimulated with 100 nM insulin for 15 min (Figures S4A–S4D). Among the four candidate signaling lipids, PGE2 (100 nM) and PGF2a (10 nM), respectively, increased insulin-stimulated $pAKT_{s473}$ under both physiological and palmitate-induced insulin-resistant conditions in HepG2 (Figure S4E), C2C12 (Figure S4F), hWAT (Figure

S4G), or hBAT cells (Figure S4H) (results are summarized in Table S2). These results point to the potency of PGE2 and PGF2a in improving insulin signaling in metabolic cells *in vitro*.

Next, we sought to identify the receptors and intracellular signaling networks that mediate the insulin-sensitizing effects of PGE2 and PGF2a. Prostaglandins are known to exert their actions by acting on G protein-coupled receptors (GPCRs).[23] There are four GPCR-designated subtypes (EP1, EP2, EP3, and EP4) that mediate the actions of PGE2.[24] Furthermore, the biological actions of PGF2a are mediated through binding with the prostaglandin F receptor (FP).[25] We therefore hypothesized that PGE2 or PGF2a exerts the insulin-sensitizing effects via binding to these receptor(s). To directly test this hypothesis, we performed independent blocking experiments by pre-treating each of the cell types with an antagonist of EP1(ONO8711),[26] EP2 (PF04418948),[27] EP3 (L826266),[28] EP4 (AH23848),[29] or FP (OBE022)[30] receptor. This was followed by treating the cells with PGE2 (100 nM) or PGF2a (10 nM) at concentrations determined from earlier experiments (Figures S4E–S4H). As a functional readout, we examined glucose uptake in the cells. Similar to the treatment for assessing insulin signaling, as described above, cells were pre-treated with specific receptor antagonist(s), followed by overnight treatment with PGE2 (100 nM) or PGF2a (10 nM) and an acute insulin stimulation (100 nM for 15 min) before assaying for 2-deoxy-glucose (2DG) uptake.

In HepG2 cells, 100 nM of PGE2 treatment induced $pAKT_{s473}$ activation independent of insulin (Figure 3F, $pAKT_{s473}$ longer exposure, and Figure S5A). Pre-treatment with EP1, EP3, or EP4 antagonists, namely, ONO8711, L826266, or AH23848, blunted the PGE2-induced $pAKT_{s473}$ even in the presence of insulin (Figures 3F and S5A). PGE2 synergistically increased $pAKT_{s473}$ without influencing pIRβ/IGF1Rβ; furthermore, inhibition of EP1 or EP4 receptor by ONO8711 or AH23848 significantly abolished the synergistic effects of PGE2 on insulin (Figures 3F and S5A). On the other hand, PGF2a did not activate $pAKT_{s473}$ per se; however, it increased insulin-stimulated $pAKT_{s473}$ likely through actions on FP receptors in liver cells, since OBE022 abolished the PGF2a-induced increase in $pAKT_{s473}$ (Figures 3G and S5B). As expected, insulin induced an increase in glucose uptake in HepG2 cells (Figure 3H). Interestingly, application of exogenous PGE2 alone induced a 1.6-fold increase in glucose uptake at 100 nM, although this uptake was not as robust as the effect of insulin in HepG2 cells (Figure 3H).

In C2C12 cells, neither PGE2 nor PGF2a increased the basal $pAKT_{s473}$ levels; however, both prostaglandins elevated insulin-stimulated $pAKT_{s473}$ (Figures 3I, S5C, and S5D). Strikingly, individual treatments with PGE2 (100 nM) or PGF2a (10 nM) led to a 2.6-fold or 3.2-fold induction of glucose uptake in C2C12 cells independent of insulin, respectively, whereas insulin on its own induced a 2-fold increase in glucose uptake as expected (Figure 3K). Simultaneous blockage of EP1 and EP2 receptors abolished PGE2-induced glucose uptake. Similarly, the use of a PF receptor antagonist significantly decreased the PGF2a-induced increase in glucose uptake in C2C12 cells (Figure 3K).

In differentiated hWAT cells, PGE2 but not PGF2a increased basal $pAKT_{s473}$ levels, and both PGs increased insulin-stimulated $pAKT_{s473}$ (Figures 3L, 3M, S5E, and S5F). Inhibition of EP2 or EP4 receptor and of FP receptor decreased PGE2- or PGF2a-induced

effects, respectively. Conversely, blockage of EP1 or EP2 receptor partially decreased the PGE2-induced effect, while the FP antagonist, OBE022, did not significantly change PGF2a-induced effects (Figures 3L, 3M, S5E, and S5F). Besides, neither PGE2 nor PGF2a affected glucose uptake in the absence of insulin, while PGE2 enhanced insulin-stimulated glucose uptake (Figure 3N).

In differentiated hBAT cells, both PGE2 and PGF2a increased insulin-stimulated $pAKT_{s473}$ without directly affecting $pAKT_{s473}$ (Figures 3O, 3P, S5G, and S5H). Interestingly, blockage of the EP4 receptor showed a significant increase in PGE2-induced $pAKT_{s473}$ (Figures 3O and S5G). On the other hand, an FP receptor antagonist completely abolished PGF2a-induced elevation in insulin-stimulated $pAKT_{s473}$ (Figures 3P and S5H). Glucose uptake in hBAT cells was significantly stimulated by insulin but was not altered in response to both PGs (Figure 3Q), suggesting that brown adipocytes are unlikely to be the major target of PGs. These data together suggest that PGE2 and PGF2a act as secretory factors that exogenously control glucose uptake primarily in muscle cells, hepatocytes, and white adipocytes.

Last, we investigated the molecular mechanism(s) activated by PGE2 or PGF2a to increase $pAKT_{s473}$. Several mechanisms exist to attenuate, fine-tune, or terminate insulin signaling, both at the level of the receptor and downstream points in the cascade.[31,32] For example, phosphatases such as PH domain and leucine-rich repeat protein phosphatases (PHLPPs), SH2 domain-containing inositol phosphatase 1/2 (SHIP-1/SHIP-2), and phosphatase and tensin homolog (PTEN) are known to negatively regulate AKT in the insulin signaling cascade.[33] We therefore hypothesized that PGE2 and PGF2a suppress the expression of specific negative regulators in the PI3K pathway and activities of pAKT. Using HepG2 cells as a model, we observed that PGE2 decreased the protein abundance of PHLPP-1, which acts to dephosphorylate AKT, and SHIP-1/2 as well as PTEN, all of which negatively regulate the PI3K pathway. Blocking EP1 or EP4 receptors partially rescued the expression of these phosphatases (Figures 3R and S5I). PGF2a decreased the protein levels of SHIP-1 and SHIP-2, and this effect was reversed by blocking the FP receptor (Figures 3S and S5J).

Taken together, four signaling lipids, namely, PGE2, PGD2, PGF2a, and 13,14-dh-15-keto-PGE2, are released by mouse or human brown adipocytes that lack *METTL14*. Among these, PGE2 and PGF2a potentially act as primary endocrine factors mediating improved peripheral insulin sensitivity. For example, PGE2 stimulates $pAKT_{s473}$ in the absence of insulin and sensitizes insulin-stimulated $pAKT_{s473}$ through distinct cell-specific EP receptors. In HepG2 cells, these actions are exerted by decreasing the expression of PHLPP-1, SHIP-1/2, or PTEN, respectively. PGF2a acts by binding with the FP receptor to negatively regulate SHIP-1 and SHIP-2 to increase insulin-stimulated $pAKT_{s473}$ (Figure 3T).

Administration of exogenous PGE2 and PGF2a improves insulin sensitivity and glucose tolerance in DIO mice

Next, we sought to study whether PGE2 or/and PGF2a are responsible for the metabolic phenotypes of $M14^{KO}$ mice. To study this, we used an anti-PGE2 monoclonal recombinant antibody (2B5) to block the effects of PGE2. The neutralizing efficacy of 2B5 was validated

in vitro using HepG2 cells, demonstrating a concentration-dependent neutralization of PGE2-induced increase in $pAKT_{s473}$ (Figures S6A–S6C). Additionally, this experiment also allowed us to consider an optimal concentration of 2B5 for the *in vivo* neutralization study.

Next, we conducted *in vivo* neutralization by injecting the control mice with isotype control immunoglobulin G (IgG) antibody and $M14^{KO}$ mice with either the control antibody or 2B5 (Figure 4A), and we validated antibody injection by determining the IgG1 level in the experimental mice (Figure S6D). As expected, $M14^{KO}$ mice injected with IgG displayed systemic improvements in insulin sensitivity (Figure 4B), glucose tolerance (Figure 4C), and hepatic insulin sensitivity (Figures 4D and 4E), compared with control mice injected with IgG. Notably, these phenotypes were virtually completely attenuated by 2B5 (Figures 4B–4E), strongly supporting that PGE2 is underlying the $M14^{KO}$ mice phenotypes. However, due to the unavailability of a commercial neutralizing antibody against PGF2a, blocking PGF2a in this experiment was not feasible.

Having identified PGs, particularly PGE2, as the insulin sensitizers responsible for the primary phenotypes of $M14^{KO}$ mice, we proceeded to directly assess the insulin-sensitizing effects of exogenous PGE2 and PGF2a in mice. However, it is worth noting that both PGE2 (12.5 mg/kg) and PGF2a (12.5 mg/kg) displayed a short plasma half-life of ~ 3.3 and ~1.4 min in the diet-induced obesity (DIO) mice, respectively (Figures S6E and S6F). Only 490 pg/mL PGE2 and 770 pg/mL PGF2a remained in circulation 2 h post-injection, indicating rapid clearance and the necessity of supraphysiological circulating concentrations to elicit observable effects *in vivo*.

Therefore, we included five groups of 13-week-old male mice for *in vivo* administration: LFD-fed groups with vehicle or 25 mg/kg PG (12.5 mg/kg PGE2 + 12.5 mg/kg PGF2a) injection and DIO mice receiving vehicle, 25 mg/kg PGs (12.5 mg/kg PGE2 + 12.5 mg/kg PGF2a), or 50 mg/kg PGs (25 mg/kg PGE2 + 25 mg/kg PGF2a) (Figure 4F). The activity, basal core body temperature, and food intake were monitored as indicators of potential side effects induced by chronic PG administration. At neither of the doses did PG administration influence the activity (Figures S6G and S6H) or basal core body temperature (Figure S6I) in the fed LFD or HFD, pointing to the safety of PG administration in mice. Besides, combined PGE2+PGF2a injection at both doses did not significantly affect the food intake (Figure S6J) or body weight, except for mice receiving 25 mg/kg PGE2+PGF2a challenged with a HFD (Figure 4G). Furthermore, DIO mice injected with the low dose of PGE2+PGF2a had smaller body sizes and decreased size and weights of iBAT, liver, iWAT, and eWAT (Figures 4H and 4I); however, these differences were not observed between the LFD-fed groups (Figures 4G, 4I, and S6K). Histological analyses of adipose tissues and liver revealed healthier morphology in the PGE2+PGF2a-injected mice on HFD (Figures 4J–4L). Specifically, the PGs decreased HFD-induced hepatic steatosis (Figure 4J), immune cell infiltration, and adipocyte hypertrophy in eWAT (Figure 4K) and iWAT (Figure 4L). Consistent with the observation on iWAT from $M14^{KO}$ mice (Figures S1J, S1S, and S1T), an induction of beige cells, indicated by multilocular morphology (Figure 4L), UCP1 positivity (Figure 4M), and the presence of browning markers (Figures 4N and 4O), was observed in the iWAT of PG-injected mice. Consistently, treating human preadipocytes with PGE2,

13,14-dh-15-keto-PGE2, PGF2a, or PGD2 induced expression of browning markers (Figure S6L).

To uncouple the insulin sensitivity from the effects of potential body weight changes, we performed IPITT on day 11 post-PGE2+PGF2a injection when body weights were similar among groups (Figure S6M). Treatment with PGE2+PGF2a did not influence LFD-fed mice, which exhibited normal insulin sensitivity while protecting DIO mice from HFD-induced insulin resistance at both doses (Figures 4P and 4Q). At the end of the experiment, PGE2+PGF2a (50 mg/kg) injection lowered the fasting glucose in HFD-fed mice (Figure 4R), and both doses of PGs decreased HFD-induced glucose intolerance (Figure 4S). Furthermore, treating DIO mice with PGs (25 mg/kg) followed by assessment of tissue level insulin sensitivity after *vena cava* insulin injection showed increased $pAKT_{s473}$ in the liver (Figure 4T) and iWAT (Figure 4U). Notably, a reduction of PHLPP1, SHIP1, and PTEN protein abundance in liver (Figure 4V) and a decrease in PHLPP1 and SHIP1 protein abundance in iWAT (Figure 4W) were observed, suggesting direct insulin sensitization via the inhibition of negative regulators of pAKT signaling.

To further understand whether the global improvement in insulin sensitivity induced by PGs was dependent on the canonical UCP1-mediated thermogenesis of BAT, we performed indirect calorimetry after acute cold exposure. Regardless of improved cold tolerance induced by both doses of PGs in the DIO mice (Figure S6N), which is likely attributed to the PG-induced iWAT browning (Figures 4M–4O), no differences were observed in energy expenditure (Figure S6O), O_2 consumption (Figure S6P), or CO_2 production (Figure S6Q) between PG- and Veh-treated groups fed with HFD after 6 h acute cold exposure. These results support the notion that $M14^{KO}$-BAT-secreted prostaglandins improve whole-body metabolism independent of BAT thermogenesis.

Collectively, long-term treatment of DIO mice with PGE2 and PGF2a phenocopied the $M14^{KO}$ mouse model and supported the concept that $M14^{KO}$-BAT improves metabolic health by endocrine effects of the PGs.

Plasma levels of PGE2 and PGF2a are negatively associated with obesity and insulin resistance in humans

Since $M14^{KO}$ mice and PGE2+PGF2a-treated mice were resistant to HFD-induced insulin resistance, we sought to examine the relevance of these findings in humans. We therefore tested the relationship between circulating levels of PGE2 or PGF2a and metabolic parameters in three independent cohorts of human subjects with a broad distribution of BMI and insulin sensitivity.

In human cohort 1, individuals are divided into lean, over-weight, and obese groups (sample information in Table S3).[9] We observed higher PGE2 levels in lean (BMI < 25 kg/m^2) compared with overweight (25 ≤ BMI < 30 kg/m^2) or obese (BMI ≥ 30 kg/m^2) groups (Figure 5A), as well as in individuals identified as BAT positive (BAT+), compared with those identified as BAT negative (BAT—) (Figure 5B). Notably, Spearman's correlation analyses revealed a significant negative correlation between plasma PGE2 levels and BMI (Figure 5C), as well as HOMA-IR (Figure 5D). Moreover, PGE2 exhibited negative

correlations with fasting plasma insulin (FPI) and leptin levels (Figure S7A). Similarly, PGF2a levels were higher in individuals who are lean than in those who are overweight or obese (Figure 5E) and in BAT+ group compared with BAT—group (Figure 5F). PGF2a also displayed inverse correlations with BMI (Figure 5G), HOMA-IR (Figure 5H), FPI, and leptin (Figure S7B). Given the known decrease in BAT mass and activity in obese humans,[34] these data support BAT as the primary source tissue of PGE2 and PGF2a in humans. The inverse correlation between PGE2 or PGF2a levels and HOMA-IR suggests that low plasma PG levels are associated with increased insulin resistance.

To further dissect the insulin-sensitizing effects of the PGs independent of BMI, we next examined the association of circulating PGE2 or PGF2a levels with the metabolic parameters in human cohort 2 (also referred to as Kuopio Obesity Surgery [KOBS] study) including only obese subjects (BMI R 30).[35] The absolute levels of PGE2 and PGF2a were measured by ELISAs. Plasma PGE2 levels did not show significant correlations with BMI (Figure 5I), which allowed us to dissect the potential effects of PGs from body weight regulation in this human cohort. Consistent with human cohort 1, we also observed a negative correlation between PGE2 and HOMA-IR in human cohort 2 (Figure 5J). In addition, PGE2 showed negative correlations with fasting glucose, insulin, and triglycerides (Figure S7C). PGF2a showed a similar pattern of correlations with the parameters mentioned above (Figures 5K, 5L, and S7D).

Finally, we proceeded to determine the relationship between circulating levels of PGE2 and PGF2a levels with peripheral insulin sensitivity. In human cohort 3 (also referred to as the Stop Diabetes [StopDia] study), where the Matsuda index that represents both hepatic and peripheral tissue sensitivity to insulin is available, we found a significantly positive correlation between PGE2 and the Matsuda index (Figure 5M). Besides, plasma levels of PGE2 were found to negatively correlate with BMI (Figure 5N), HOMA-IR (Figure 5O), and FPI (Figure S7E), respectively. Similarly, the PGF2a level was positively correlated with the Matsuda index (Figure 5P), while being negatively correlated with other parameters mentioned above (Figures 5Q, 5R, and S7F). Overall, these findings suggest that PGE2 and PGF2a are linked to systemic metabolism and insulin sensitivity in humans.

METTL14 deficiency upregulates pathways related to prostaglandin synthesis in BAT

To answer the lingering question regarding the mechanism(s) by which *METTL14* regulates prostaglandin synthesis in brown adipocytes, we began by determining the transcriptional basis of prostaglandin synthesis following *METTL14* ablation. We performed RNA sequencing (RNA-seq) and m^6A-RNA immunoprecipitation sequencing (m^6A-RIP-seq) in iBAT from control or $M14^{KO}$ mice (Figure 6A). Principal-component analysis (PCA) of both RNA-seq and m^6A-seq data showed a clear separation between control- and $M14^{KO}$-iBAT (Figures 6B and 6C, respectively). RNA-seq identified 697 differentially expressed genes (DEGs) ($p < 0.01$) in $M14^{KO}$-iBAT consisting of 324 upregulated and 373 downregulated genes (Figure 6D). Pathway and process enrichment analyses of the significantly upregulated genes revealed the metabolism of lipids and phospholipid metabolic process among the top upregulated pathways as a consequence of *Mettl14* deficiency (Figures 6E and S8A). Consistently, pathways including response to insulin,

adipogenesis, and glucose homeostasis were upregulated in M14^{KO}-iBAT, compared with controls. On the other hand, top-ranking ontologies for the downregulated genes were related to angiogenesis, cell cycle, and mitosis (Figure S8B).

As previously reported,[36,37] the m^{6}A peaks in both control- and M14^{KO}-iBAT were enriched at the start and stop codons and were characterized by the canonical GGACU motif (Figure S8C). To further test whether the transcriptomic alterations related to the phospholipid synthesis pathways were regulated by METTL14-mediated m^{6}A decoration, we intersected the differentially upregulated ($p < 0.05$) and m^{6}A-hypomethylated genes ($p < 0.05$) and obtained 714 transcripts (Figure 6F). Consistent with our RNA-seq data, this group of 714 genes was the most enriched for the phospholipid metabolic process and metabolism of lipid pathways (Figures 6G and S8D).

Prostaglandin synthesis occurs when a cyclooxygenase enzyme (Cox1 and Cox2, also known as Ptgs1 and Ptgs2, respectively) converts arachidonic acid to an intermediate that is subsequently converted to an active prostanoid such as PGE2 and PGF2a. The biosynthesis of diverse PGs from arachidonic acid is directly enabled by PG synthases such as the prostaglandin E synthases (PTGES, PTGES2, and PTGES3) but also indirectly regulated by several transcription regulators or transcriptional coactivators.[38,39] To further identify the target transcripts of METTL14 involved in the PG biosynthesis pathway, we analyzed the m^{6}A levels of the genes encoding prostaglandin biosynthesis enzymes in control- and M14^{KO}-iBAT. Several genes involved in the PG biosynthesis pathway were highly hypomethylated in the M14^{KO}-iBAT (Figure 6H). More specifically, prostaglandin E synthase 2 (*Ptges2*) (Figure 6I), which encodes the synthase for PGE2 synthesis; carbonyl reductase 1 (*Cbr1*) (Figure 6J); and aldo-keto reductase family 1 member B10 (*Akr1b10*) (Figure 6K), which are responsible for the production of PGF2a and 13,14-dh-15-keto-PGE2, showed lower m^{6}A levels. Other hypomethylated genes in this pathway included peroxisome proliferator-activated receptor gamma (*Pparγ*) (Figure 6L), which promotes the synthesis/release of PGE2[39]; peroxisome proliferative activated receptor gamma coactivator 1 alpha (*Ppargc1α*) (Figure 6M), which promotes the expression of prostaglandin-endoperoxide synthase 1 (*Ptgs1*)[38]; and peroxisome proliferative activated receptor gamma coactivator 1 beta (*Ppargc1β*) (Figure 6N), which is a known regulator of several prostaglandin synthases. Among other hypomethylated genes in M14^{KO}-iBAT were endothelin receptor type A (*Ednr*a) (Figure 6O); phospholipase A2, group XIIA (*Pla2g12α*) (Figure 6P), which induces liberation of arachidonic acid from cellular membranes; as well as 11b-hydroxysteroid dehydrogenase type 1 (*Hsd11b1*) (Figure 6Q), which promotes conversion of arachidonic acid into prostaglandin H2 (PGH2) (Figure 6H). Thus, these three transcripts might contribute to the production of prostaglandins by providing additional substrates (i.e., arachidonic acid and PGH2). Consistently, enriched pathways and genes were also observed in the sgM14-hBAT cells (Figures S8E and S8F). Overall, these results indicate that a deficiency of *METTL14*, directly and indirectly, regulates the synthesis of prostaglandins in mouse and human brown adipocytes.

METTL14-mediated m^{6}A installation promotes the mRNA decay of prostaglandin biosynthesis enzymes and their regulators in an YTHDF2/3-dependent manner

We proceeded to validate our sequencing findings and explore the molecular mechanisms underlying METTL14-mediated m^{6}A modification of target transcripts in the PG synthesis pathway. Initially, RT-qPCR analyses confirmed the upregulation of *Pparγ*, *Ppargc1α*, *Ppargc1β*, *Ptges2*, *Crb1*, and *Akr1b10* in M14^{KO}-iBAT (Figure 7A). Interestingly, although no changes were detected in the m^{6}A levels within the transcripts of *15-Pgdh* and *Ptgds*, their gene expression was upregulated in M14^{KO}-iBAT (Figure S9A), suggesting that they are not direct targets of METTL14-mediated m^{6}A. Furthermore, the protein levels of PPARγ, PGC1α, PGC1β, PTGES2, CBR1, and AKR1B10 were increased in the iBAT of M14^{KO} mice (Figures 7B and S9B). Consistently, gene expression (Figures 7C and S9C) and protein levels (Figures 7D and S9D) of PG biosynthesis enzymes and their positive regulators were increased in sgM14-hBAT cells.

We then took advantage of the hBAT cell model to conduct mechanistic studies. First, we examined the effects of *METTL14* deficiency on the stability of candidate target mRNAs following treatment with actinomycin D (Act D), an inhibitor of transcription, in hBAT cells. *METTL14* deficiency did not significantly affect the stability of *ACTB* mRNA; however, it potently suppressed the degradation of *PTGES2*, *CBR1*, and *AKR1B10* mRNAs in the differentiated hBAT cells (Figure 7E). These data suggest that METTL14-mediated m^{6}A methylation regulates target mRNA levels by influencing their stability.

To confirm this hypothesis, we performed small interfering RNA (siRNA)-mediated knockdown of the m^{6}A reader proteins YTHDF2 and YTHDF3 (Figure 7F), which are important for mRNA stability,[11,13] and examined the expression and stability of *PTGES2*, *CBR1*, and *AKR1B10* mRNAs after ActD treatment in wild-type hBAT cells. Knockdown of either YTHDF2 or YTHDF3, followed by ActD treatment, did not affect the stability of *ACTB* but increased the stability of *PTGES2*, *CBR1*, and *AKR1B10* mRNAs (Figure 7G). In the chase experiment with the translation inhibitor cycloheximide (CHX), *METTL14* deficiency did not alter GAPDH protein expression over 12 h, likely due to its long half-life (Figures 7H and S9E). Additionally, METTL14 deficiency did not significantly affect the translational efficiency of *PPARγ*, *PGC1α*, *PGC1β*, *PTGES2*, *CBR1*, and *AKR1B10* mRNAs in hBAT cells (Figures 7H and S9E), suggesting that METTL14 primarily regulates transcriptional processes rather than translational efficiency.

METTL14 overexpression (M14OE) (Figures S9G and S9H) in hBAT did not affect adipogenesis (Figure S9F) but decreased gene expression of *PPARγ*, *PGC1α*, *PGC1β*, *PTGES2*, *CBR1*, and *AKR1B10* (Figure S9H). M14OE promoted *PTGES2*, *CBR1*, and *AKR1B10* mRNA degradation in hBAT cells post-ActD treatment (Figure S9I) and reduced secretion of PGE2 and PGF2a (Figure S9J). Additionally, M14OE-hBAT-conditioned media lowered pIRβ/IGF1Rβ and pAKT$_{s473}$ levels in HepG2 (Figure S9K) and hWAT cells (Figure S9L) pre-treated before insulin stimulation, compared with controls.

Finally, having identified *Ptges2* and *Cbr1* as the key target transcripts of M14-mediated m^{6}A, encoding PGE2 and PGF2a biosynthesis enzymes, respectively (Figure 7I), we aimed to elucidate the significant contributions of *Ptges2* and *Cbr1* to enhanced insulin sensitivity.

AAV8-scramble, AAV8-shPtges2, or AAV8-shCbr1 were injected into iBAT to genetically knock down *Ptges2* or *Cbr1* specifically (Figure 7J). Knockdown efficiency and tissue specificity were confirmed by reduced PTGES2 and CBR1 protein abundance exclusively in iBAT (Figures 7K, 7L, S9M, and S9N). Knockdown of each gene notably decreased plasma PGE2 and PGF2a levels in $M14^{KO}$ mice (Figure 7M), affirming PTGES2 and CBR1 as a key enzyme for PGE2 and PGF2a biosynthesis, respectively. Notably, *Ptges2* depletion virtually abolished improved systemic insulin sensitivity and glucose tolerance in $M14^{KO}$ mice (Figures 7N and 7O), likely due to PGE2's role as a precursor to PGF2a and 13,14-dh-15-keto-PGE2.[40] *Cbr1* knockdown partially reversed this phenotype (Figures 7N and 7O). Consistently, insulin sensitivity was also observed at the tissue level, particularly in the liver (Figures 7P and 7Q). These results confirm *Ptges2* and *Cbr1* as key targets of M14-mediated m^6A in brown adipocytes, underscoring BAT-secreted PGE2 and PGF2a as major drivers of the improved insulin sensitivity in $M14^{KO}$ mice.

Collectively, we have uncovered a unique mechanism by which BAT regulates systemic insulin sensitivity in peripheral metabolic tissues. Our findings indicate that METTL14 deficiency selectively induced hypomethylation in transcripts encoding prostaglandin biosynthesis enzymes, consequently inhibiting their mRNA decay. This leads to an upregulation of prostaglandin production within brown adipocytes.

DISCUSSION

Insulin resistance, which is characterized by reduced sensitivity to insulin in several metabolic tissues, is known to be associated with glucose intolerance and type 2 diabetes (T2D). The activity of BAT has been found to negatively correlate with body BMI[34,41] while being positively associated with insulin sensitivity.[41] Therefore, targeting BAT, particularly its secretory functions, presents one potential approach for the prevention and treatment of obesity and insulin resistance.[4,42]

BAT secretes various bioactive factors that can either directly modulate brown adipocyte insulin sensitivity and/or, importantly, act as endocrine factors to regulate insulin sensitivity in peripheral metabolic tissues independent of canonical thermogenesis. Some of these factors include proteins (e.g., Nrg4,[43] FGF21,[44] FGF6, and FGF9),[45] signaling lipids or so-called lipokines such as 12,13-di-HOME,[7,8] and omega-3 oxylipin 12-HETE.[9] Exosomal microRNAs have also been reported to regulate systemic metabolism by interorgan crosstalk.[46–48] However, most of these factors have been reported to be released in response to cold stimulation,[7,9,10,45,49] browning inducers,[50] or exercise,[8] and there is an urgent need to identify novel strategies for regulating the BAT secretome. Here, we describe a unique mechanism by which METTL14-mediated m^6A mRNA methylation negatively regulates the synthesis of BAT signaling lipids, i.e., prostaglandins. *Mettl14* deficiency in BAT enhances systemic insulin sensitivity independently of body weight changes and, notably, independent of UCP1-mediated canonical BAT thermogenesis. Instead, *Mettl14* deficiency promotes the secretion of BAT-produced PGE2 and PGF2a, which act as effective insulin sensitizers. The mechanism of PGE2 and PGF2a action is intriguing: without significantly affecting pIRβ/IGF1Rβ level in peripheral metabolic tissues, both lipids activate $pAKT_{s473}$ by inhibiting specific negative regulators of pAKT.

Interestingly, UCP1 is downregulated in M14^{KO}-iBAT. This finding, along with unaltered energy expenditure and the maintained phenotypes under cold or thermoneutral conditions, points to the notion that the improved insulin sensitivity is mediated via a UCP1-independent mechanism. However, further research employing UCP1-deficient models is needed to directly validate this hypothesis. Considering that the anti-obesity effects of UCP1-dependent thermogenesis are only supported by a proof-of-principle study in UCP1-knockout (Ucp1^{KO}) mice maintained at thermoneutrality[51]; and that obese and aging humans express minor amounts of UCP1 and most do not live in thermoneutral conditions,[52] UCP1-independent mechanism(s) in BAT, such as its endocrine functions, may hold significant translational relevance.

Another interesting observation in M14^{KO} mice is the improved cold tolerance. Despite the significant downregulation of *Ucp1* gene expression and protein abundance in BAT, a beige phenotype was observed in the iWAT of M14^{KO} mice, suggesting white-to-brown adipose tissue conversion as a compensatory response to the reduced UCP1 level in BAT. As discussed previously, several PGs, including PGE2 and PGD2, are known as browning inducers through various mechanisms.[45,53,54] PGE2 interacts with PPARγ to divert preadipocyte differentiation into beige adipocytes,[55,56] while PGD2 promotes *de novo* beige adipocyte biogenesis through stimulating CD81+ progenitor cell proliferation in a paracrine or autocrine manner via the receptor DP1.[54] This led us to hypothesize that the white-browning phenotype is induced by the elevated levels of PGs. Indeed, PGE2, PGD2, 13,14-dh-15-keto-PGE2, or PGF2a treatment during the late differentiation stage induced PGC1α and UCP1 protein expression in hWAT cells. Consistently, exogenous PGE2 and PGF2a administration in mice markedly induced the formation of beige adipocytes in their iWAT. These data support a previously unreported observation showing the browning-inducing effect of PGF2a and 13,14-dh-15-keto-PGE2. However, future studies should confirm this observation and elucidate the mechanism(s) by which these two PGs promote conversion from white-to-brown fat.

Importantly, the translational relevance of our *in vitro* and animal studies is demonstrated by the inverse correlations observed between circulating PGE2 or PGF2a levels and HOMA-IR in three independent human cohorts. Notably, plasma from individuals who are BAT+ displayed higher levels of PGE2, PGF2a, and 13,14-dh-15-keto-PGE2, compared with individuals identified as BAT—. This finding strongly points to BAT as a primary source tissue for PGE2/PGF2a as well as their metabolites in humans, highlighting its importance in regulating prostaglandin levels and its potential implications on systemic metabolism in humans.

The transcriptome and m^{6}A methylome analyses indicate that the deficiency of *METTL14* leads to an upregulation in the metabolism of lipids and the phospholipid metabolism pathway. However, a key question remains: how does METTL14-mediated m^{6}A regulation specifically affect the biosynthesis of prostaglandins in brown adipocytes? The biosynthesis of prostaglandins involves the sequential oxygenation of arachidonic acid by cyclooxygenases (COX1 and COX2) to form PGH2. Specific PGs are then formed through the actions of different terminal PG biosynthesis enzymes on PGH2 (Figure 6H). It is worth noting that several transcription factors and coactivators, such as

PPARγ, PGC1α, and PGC1β, can each regulate the activity of terminal PG synthases. Therefore, we focused specifically on the genes encoding PG biosynthesis enzymes and their regulators. Our analyses revealed that the *Ednra*, *Pla2g12a*, and *Hsd11b1* genes were hypomethylated and upregulated in the $M14^{KO}$-iBAT. EDNRa and PLA2G12α enzymes are responsible for promoting the synthesis of arachidonic acid, while the HSD11B1 enzyme-promoted regeneration of COX2 contributes to the production of PGH2.[57] More substrates (arachidonic acid and PGH2) are likely released/converted for the subsequent conversion into specific PGs. *Mettl14* deficiency results in the upregulation of enzymes involved in the conversion of PGE2, PGD2, PGF2a, and 13,14-dh-15-keto-PGE2 in brown adipocytes through direct and indirect regulation. First, the transcripts encoding enzymes PTGES2 (PGE2 synthase), CBR1, and AKR1B10 (PGF2a biosynthesis enzymes) were upregulated and m^6A hypomethylated, suggesting direct regulation by m^6A. Second, transcription factors/coactivators *Pparγ* and *Pgc1α* were also upregulated and m^6A hypomethylated, potentially leading to the indirect upregulation of genes encoding PTGDS (PGD2 synthase) and 15-PGDH (13,14-dh-15-keto-PGE2 intermediate biosynthesis enzyme) proteins.[38,39] Overall, these findings suggest that *Mettl14* deficiency directly and indirectly upregulates the expression of enzymes involved in prostaglandin conversion in brown adipocytes.

A recent publication using $Mettl14^{fl/fl}$-$Adipoq^{cre}$ mouse model to induce *Mettl14* knockout in both WAT and BAT suggested that *Mettl14* deficiency-induced WAT lipolysis plays a central role in the improved whole-body metabolism.[58] In contrast, our study uses $Mettl14^{fl/fl}$-$Ucp1^{cre}$ to specifically knockout *Mettl14* in BAT, revealing BAT-secreted PGs as the pivotal drivers of the phenotypes. Notably, despite the significant role of Mettl14 in regulating lipolytic genes in WAT, as reported in their study, our examination of $M14^{KO}$-iBAT revealed no alteration in the expression of these genes or protein abundance (data not shown). These findings underscore the conceptual differences between our work and the published study.

In conclusion, this study reveals a unique role of m^6A modification in the regulation of BAT secretory function. The BAT-secreted prostaglandin action represents an unexpected lipid-induced signaling pathway with beneficial metabolic effects in multiple key metabolic tissues. These insights offer a potential therapeutic avenue for the prevention and treatment of insulin resistance, supporting the notion of targeting m^6A modification to develop novel agents for the treatment of metabolic diseases.

Limitations of the study

There are some limitations to this work. First, BAT-secreted factors include proteins, lipids, and exosomal miRNAs. In this study, we ruled out a major regulatory role of proteins by denaturing the conditioned media; however, we cannot completely exclude potential regulation by miRNAs. Indeed, m^6A has been reported to regulate miRNA biosynthesis by participating in the processing of pre-miRNAs or splicing of pre-miRNAs, and our RNA-seq and m^6A-seq suggested many genes being regulated by miRNAs. Therefore, a future study should investigate the miRNA profile in the $M14^{KO}$-BAT and its subsequent role in the regulation of insulin sensitivity. Second, while PGE2 and/or PGF2a treatment protected mice from HFD-induced gain in body weight and corrected insulin resistance and glucose

intolerance, it is important to note that future studies should benchmark the efficacy of PGE2 and PGF2a to other anti-diabetic drugs that have been reported to have high efficacy in mice, including thiazolidinediones. Third, both our M14^{KO} mice and the PG-treated mice were less prone to DIO, while their energy expenditure and food intake were comparable with controls. Given the fact that the Ucp1^{KO} mice are resistant to DIO via secreting energy-storing metabolites in urine,[44] and M14^{KO}-BAT has downregulated *Ucp1* expression, additional studies are warranted to explore whether these mice secrete energy into their feces and/or urine.

RESOURCE AVAILABILITY

Lead contact—Further information and requests for resources and reagents should be directed to and will be facilitated by the lead contact, Rohit N. Kulkarni (rohit.kulkarni@joslin.harvard.edu).

Materials availability—This study did not generate new unique reagents.

Data and code availability

- m^{6}A-sequencing and RNA-sequencing datasets in mouse brown adipose tissue have been deposited with the National Center for Biotechnology Information Gene Expression Omnibus under accession code GSE232491.
- This paper does not report the original code.
- Source data reported in this paper are provided in Data S1.
- Any additional information required to reanalyze the data reported in this paper is available from the lead contact upon request.

STAR★METHODS

EXPERIMENTAL MODEL AND SUBJECT DETAILS

Mouse models and treatment—*Mettl14*$^{fl/fl}$ mice on a C57BL/6N background[14] were crossed with *Ucp1*^{cre} strain (stock no.024670, the Jackson Laboratory) mice, which do not harbor the nicotinamide nucleotide transhydrogenase (Nnt) mutation, to generate the knockouts.

For studies on diet-induced obesity and long-term insulin resistance, control and M14^{KO} mice were fed either 10% fat LFD or a conventional 60% fat HFD for 16 weeks, starting at 4 weeks of age.

To examine tissue-specific insulin sensitivity, control and M14^{KO} mice were fasted for 16 hours. After being anesthetized, 1 U of insulin was injected directly into the *vena cava*.[21] Tissues were harvested at the indicated time points as shown in Figure 2A.

db+ and *db/db* (BKS.Cg-Dock7<m>+/+Lepr<db>/J) mice were purchased from The Jackson Laboratory (Strain 000642). Adipose tissues were collected for the assessment of m^{6}A regulator protein abundance by Western blot analysis at 10 weeks of age.

Acute or chronic cold, and thermoneutral exposure—For cold tolerance tests, control and M14^{KO} mice were cased individually at 5 °C in temperature-controlled diurnal incubators (Caron Products and Services) for 1 to 6 hours, with free access to water and food. Core body temperature was monitored hourly via rectal measurements. For chronic cold exposure, 10-week-old male mice experienced intermittent cold exposure (12 hours at 5 °C during the light cycle and 12 hours at room temperature (22 °C)) for 3 days, followed by 4 days of continuous cold exposure at 5 °C. IPITT and IPGTT were conducted on days 1 and 4 post chronic cold exposure. Similarly, for thermoneutrality exposure, 10-week-old male mice were continuously housed at 30 °C in temperature-controlled diurnal incubators. IPITT and IPGTT were performed on days 1 and 4 post chronic thermoneutrality exposure. Throughout both chronic cold and thermoneutrality exposures, mice had ad libitum access to food and water.

***In vivo* administration of PGE2 and PGF2a—**To assess the half-life of PGE2 and PGF2a in the DIO mice, and determine the concentrations for further *in vivo* administration, we performed a pharmacokinetic study by co-injecting the 20 weeks of male DIO mice with 12.5 mg/kg PGE2 and 12.5 mg/kg PGF2a and detect the remaining PGs in the plasma at different timepoints before (as basal level) and after injection.

For chronic treatment with PGs, mice were mock injected with saline for three days before administering PGE2 and PGF2a to prevent stress-induced weight loss. Mice were then injected via the intraperitoneal route with vehicle (saline), or 12.5 mg/kg of PGE2 and 12.5 mg/kg PGF2a (labeled as 25 mg/kg PGE2+PGF2a), or 25 mg/kg of PGE2 and PGF2a (labeled as 50 mg/kg PGE2+PGF2a) every other day for 3 weeks. Body weight was measured weekly. IPITT and IPGTT were performed on day 11 and day 21 post-treatment. Indirect calorimetry was performed on day 16 post-treatment after acute cold exposure. At the end of the experiment, tissues were collected after *vena cava* insulin injection as described before in mouse models and treatment section.

***In vivo* neutralization experiment—**Control mice were subjected to intraperitoneal (i.p.) injection of the control antibody IgG. Meanwhile, M14^{KO} mice were randomly assigned to two groups: one receiving mouse IgG1 isotype control antibody (Creative Biolabs, CAT#: MOB-065CQ-LowE) and the other receiving anti-PGE2 monoclonal recombinant antibody (2B5) (Creative Biolabs, CAT#: TAB-1022CL) at a dosage of 250 μg per mouse, administered every other day over 16 days. To validate the presence of antibodies, mouse IgG1 was measured in the plasma using a mouse IgG1 ELISA kit (Thermo Fisher Scientific, CAT#: 88–50410-22). IPITT was conducted on day 10 following neutralization, while IPGTT was performed on day 16 post-neutralization. At the end of the experiment, tissues were collected after *vena cava* insulin injection as described before in the mouse models and treatment section.

Reverse experiment with AAV8 vectors—To achieve specific knockdown of *Ptge2* or *Cbr1* in the iBAT of M14^{KO} mice, four groups of mice were included: control mice received injections of AAV8-eGFP (referred to as AAV-scramble), while M14^{KO} mice were randomly divided into three groups. One group received AAV8-eGFP (AAV-scramble, VectorBuilder, CAT#: AAV8MP(VB010000–0023jze)-C), while the other two groups were

injected with AAV8 vectors designed to knock down either *Ptges2* (AAV8-shPtges2, VectorBuilder, CAT#: P230909–1024kae) or *Cbr1* (AAV8-shCbr1, VectorBuilder, CAT#: P230909–1025vez). The procedure for BAT-specific AAV injection using Hamilton syringes was previously detailed.[61] Briefly, each mouse received a total of 30 μL (10^13 genome copies (GC/mL)) of AAV solution, administered into the interscapular BAT (iBAT) with 15 μL of AAV solution distributed across three injection sites within each iBAT lobe. Knockdown was verified by WB. IPITT was conducted at 4 weeks post-AAV injection, while IPGTT was performed at 5 weeks post-AAV injection. At the end of the experiment, tissues were collected after *vena cava* insulin injection as described before in mouse models and treatment section.

Studies on molecular, cellular, and genetic characterization of human adipose tissue and its role in metabolism—Brown adipose tissue samples from 13 adult (6 males and 7 females) participants were selected from a cohort of healthy volunteers and surgical patients known to have brown adipose tissue, identified by PET/CT (ClinicalTrials.gov Identifier: NCT02692885). Brown adipose tissues were collected from different depots including retroperitoneal, deep abdominal, deep periadrenal, and deep retroperitoneal depots. Samples were divided into non-obese (BMI< 30) or obese (BMI ≥ 30) groups. Donor information is summarized in Table S1. qRT-PCR was performed to detect the gene expression of m^6A writers, erases, and readers.

Studies related to lean and obese human subjects (human cohort 1)—As described previously,[9] a group of 55 people was selected from the Leipzig obesity biobank to represent a wide range of BMI and parameters of glucose metabolism. This group consisted of 42 women and 13 men with BMI ranging from 17.5 to 75.4 kg/m^2. The group was divided into 3 subgroups: lean (n=15), overweight (n=13), and obese (n=27). In the lean subgroup, all individuals were normal glucose tolerant, while in the overweight subgroup, 10 were normal glucose tolerant and 3 had T2D, and in the obese subgroup, 20 were normal glucose tolerant and 7 had T2D. Patient information is summarized in Table S3. The collection of human biomaterial, serum analyses, and phenotyping was approved by the ethics committee of the University of Leipzig (approval numbers: 159–12-21052012 and 017–12-23012012) and all individuals provided written informed consent.

Studies related to obese human subjects of KOBS (human cohort 2)—As described previously,[35] this study used data from 175 individuals with obesity (BMI ≥ 30) in the Kuopio Obesity Surgery (KOBS) Study (patient information is summarized in Table S4). PGE2 and PGF2a were measured by the Prostaglandin E2 Express ELISA Kit and Prostaglandin F2a ELISA Kit, respectively (Cayman Chemical, Ann Arbor, MI) according to the manufacturer's instructions. For the correlation analysis, Box-Cox transformation on the values of metabolites (PGE2 and PGF2a) and clinical variables (BMI, triglycerides, fasting glucose, fasting insulin, HOMA-IR, and liver steatosis/NASH histology grades), which was appropriate for reducing skewness and to approximate normality (Box 1964) was performed. The bagged trees method was used for data imputation. Briefly, for each variable in the data, a bagged tree was created using all of the other variables. When a new sample

has a missing variable value, the bagged model is used to predict the value. In theory, this is a powerful method of imputing.

Studies related to StopDia (human cohort 3)—Plasma samples were obtained from 73 individuals in the Stop Diabetes (StopDia) Study as described previously[59] (patient information is summarized in Table S5). Briefly, overnight (12 hours) fasting blood samples were obtained and analyzed for glucose and insulin concentrations [fasting and 2 hours after the ingestion of 75 g glucose in an oral glucose tolerance test, glycated hemoglobin (HbA1c)] and fasting plasma total and lipoprotein lipid concentrations [total cholesterol, low-density lipoprotein (LDL) cholesterol, high-density lipoprotein (HDL) cholesterol and total triglycerides]. Matsuda index, as a measure of peripheral insulin sensitivity, was calculated using commonly used formulas. PGE2 and PGF2a were measured by the Prostaglandin E2 Express ELISA Kit and Prostaglandin F2a ELISA Kit, respectively (Cayman Chemical, Ann Arbor, MI) according to the manufacturer's instructions.

Human brown adipocyte culture and differentiation—Immortalized human preadipocytes[60] were cultured in high-glucose DMEM containing 10% FBS. When cells reached confluence, brown adipocyte differentiation was induced by using an induction medium (DMEM high-glucose medium with 10% FBS, 33 μM biotin, 17 μM pantothenate, 0.5 μM human insulin, 500 μM IBMX, 2 nM T3, 0.1 μM dexamethasone and 30 μM indomethacin) for 21 days. Once fully differentiated, cells were washed with PBS, and RNA and protein were extracted for qRT-PCR and western blot analyses, respectively.

Human white adipocyte culture and differentiation—For differentiation of human white adipocytes, immortalized human preadipocytes[60] were induced using the same protocol and induction medium as described above for 14–18 days. Fully differentiated hWAT cells were co-cultured with freshly collected hBAT conditioned-medium, and protein was extracted for western blot analysis.

Primary human myoblast culture and differentiation—Primary GIBCO Human Skeletal Myoblasts (Thermo Fisher Scientific) were thawed and plated in DMEM supplemented with 2% horse serum. Cells were differentiated for 48 hours to form myotubes before being co-cultured with freshly collected hBAT conditioned-medium.

Primary human hepatocyte culture—Primary hepatocytes pooled from '5-Donor' human hepatocytes (Thermo Fisher Scientific) were thawed and cultured in William's E medium supplemented with primary hepatocyte supplements (Thermo Fisher Scientific) and HepExtend supplement (Thermo Fisher Scientific). Cells were washed with PBS and co-cultured with freshly collected hBAT conditioned medium.

Cell line culture and differentiation—HepG2 human hepatocytes were purchased from ATCC and cultured with 5.5mM low glucose DMEM medium (Gibco) supplemented with 10% FBS, 1% penicillin, and 1% streptomycin in a humidified 5% CO_2 incubator at 37 °C for 3 days to achieve 70% confluence before treatment.

C2C12 mouse skeletal myoblast cells were purchased from ATCC and cultured according to the manufacturer's recommendations. When cells reached an 80–90% confluence they were induced to differentiate, by altering the growth medium to differentiation medium which consisted of DMEM medium, 5% HS (Horse Serum, Gibco, 16050114), and 1% P/S under the same culture environment.

Cell treatments

hBAT-conditioned media co-culture experiments: hBAT cells were differentiated for 21 days, washed with PBS, and cultured in 1% BSA containing high-glucose DMEM medium for 24 hours. Fresh conditioned media were collected for co-culture experiments. hBAT cells were stimulated with 100 nM of insulin for 15 min and cell pellets were collected for protein and RNA extraction (Figure 2G). Fresh conditioned media were used for treating fully differentiated hWAT, primary human hepatocytes, and differentiated human myotubes for 16 hours (Figure 2G). Recipient cells were washed with PBS and stimulated with 100 nM of insulin for 15 min and cell pellets were collected for protein extraction.

PG treatments: Overnight starved HepG2 cells (Figure S4A), differentiated C2C12 myotubes (Figure S4C), fully differentiated hWAT cells (Figure S4E), and fully differentiated hBAT cells (Figure S4G) were treated with 10, 100, 1000 nM of PGE2, PGD2, PGF2a, or 13,14-dh-15-keto-PGE2 overnight in the presence or absence of 500 nM of palmitate. Cells were washed with PBS and treated with 100nM of insulin for 15 min, cell pellets were collected for protein extraction.

PGE2 and PGF2a treatment with receptor antagonists: Overnight starved HepG2 cells, differentiated C2C12 myotubes, differentiated hWAT cells, and differentiated hBAT cells were pretreated with 60 nM of ONO8711 (EP1 antagonist), 1600 nM of PF04418948 (EP2 antagonist), 80 nM of L826266 (EP3 antagonist), or 26 μm of AH23848 (EP4 antagonist) for 1hr, followed by 100 nM of PGE2 treatment overnight. In parallel, cells were pre-treated with 26 nM of OBE022 (FP antagonist) for 1hr before treatment with 10 nM of PGF2a. Cells were washed with PBS and stimulated with insulin (100 nM) for 15 min and collected for protein extraction. Except for OBE022 (purchased from MedChemExpress), all the antagonists were purchased from Cayman Chemical.

***In vitro* PGE2 neutralization assay—**HepG2 cells were pretreated with control antibody IgG (100μg) or different concentrations of 2B5 (1μg, 10μg, or 100μg) for 2 hours, followed by treatment with 100nM PGE2 overnight before exposure to 100nM insulin for 15 minutes. Cells were then stimulated with insulin or 1% BSA for 15 minutes and harvested for western blot analysis for insulin signaling.

Actinomycin D treatment: Differentiated sgNTC- and sgM14-hBAT cells were treated with 100μg/mL Actinomycin D (Thermo Fisher) or DMSO for 0, 3, 6, or 12h. Differentiated Lenti-Control and M14OE-hBAT cells were treated with 100μg/mL Actinomycin D (Thermo Fisher) or DMSO for 0, 3, 6, or 12h.

Cycloheximide treatment: Differentiated sgNTC- and sgM14-hBAT cells were treated with 100 μg/mL Cycloheximide (CHX) or DMSO for 0, 6, or 12 h, and cell pellets were collected for protein extraction.

Transfections

Knock-out experiments: To generate stable M14 knockout in hBAT preadipocytes, three different Edit-R All-in-one Lentiviral human *METTL14* single guide RNA (sgM14) and a Non-targeting control single guide RNA (sgNTC) was purchased from Horizon Discovery. After lentiviral transduction, hBAT preadipocytes were selected by puromycin treatment for 6 days to establish stable $M14^{KO}$ cell lines for adipocyte differentiation and functional experiments. Knockouts were validated by both qRT-PCR and western blot analyses.

Knock-down experiments: For transient knockdown of YTHDF1/2/3, differentiated hBAT cells were mixed with Lipofectamine RNAiMAX Reagent (Life Technologies) and small interfering RNA complexes (Dharmacon) at a final concentration of 15 nmol/L siRNA according to manufacturer instructions. ON-TARGETplus Non-Targeting Control Pool D-001810–10-05, ON-TARGETplus Human YTHDF1 siRNA L-018095–02-0005, ON-TARGETplus Human YTHDF2 siRNA L-021009–02-0005, ON-TARGETplus Human YTHDF3 siRNA L-017080–01-0005 (Dharmacon, USA). Transfected hBAT cells were treated with 100μg/mL Actinomycin D (Thermo Fisher) or DMSO 72h post-transfection.

Overexpression experiments: For stable overexpression of *METTL14* in hBAT preadipocytes, control, and *METTL14* overexpression lentiviral plasmids were designed. Overexpression was validated by both qRT-PCR and western blot analyses. Stable overexpression hBAT preadipocytes were expanded and differentiated for experiments including insulin stimulation, co-cultured experiments, and Actinomycin D treatment.

METHOD DETAILS

Glucose and insulin tolerance tests—For glucose tolerance tests, mice were fasted overnight and injected via the intraperitoneal (I.P). route with glucose (2 g/kg body weight). Blood glucose levels were measured before 0 min, and 15, 30, 45, 60, 90, and 120 mins after injection. For insulin tolerance tests, mice were fasted for 6 hours and injected I.P. with 1U/kg insulin. Blood glucose levels were measured before 0 min, or 15, 30, 45, 60, and 90 mins after injection.

Food intake, energy expenditure, and body composition measurements—For measuring daily food intake, mice were caged individually, and the amount of feed was weighed and recorded before and after a 24-hour interval. Daily food intake = the weight of feed provided – rest of the feed after 24 hr.

For indirect calorimetry, mice were individually housed in metabolic cages of a Comprehensive Lab Animal Monitoring System (CLAMS) at room temperature. After a 12h acclimation period, animals were exposure to acute cold exposure as described above in the acute or chronic cold and thermoneutral exposure section and then monitored for 72h to obtain energy expenditure measurements, the volume of oxygen consumption (VO_2), and the

volume of carbon dioxide production (VCO_2). Body composition including total mass, fat mass, and lean mass was measured by Dual-energy X-ray absorptiometry (DEXA) scan, and lean mass was used for CLAMS outcome normalization.

RNA isolation and quantitative RT-PCR—High-quality total RNA (>200nt) was extracted using standard Trizol reagent (Invitrogen) according to manufacturer's instructions and the resultant aqueous phase was mixed (1:1) with 70% RNA-free ethanol and added to Qiagen Rneasy mini kit columns (Qiagen) and the kit protocol was followed. RNA quality and quantity were analyzed using Nanodrop 1000 and used for reverse transcription using the high-capacity cDNA synthesis kit (Applied Biosciences). cDNA was analyzed using the ABI 7900HT system (Applied Biosciences) and gene expression was calculated using the $^{\Delta\Delta}$Ct method. Data was normalized to the expression of housekeeping genes. The sequences of primers used in this study are provided in Table S6.

Western blots and molecular analyses—Total proteins were harvested from tissue and cell lines lysates using M-PER protein extraction reagent (Thermo Fisher) and supplemented with proteinase and phosphatase inhibitors (Sigma), respectively, according to standard protocol. Protein concentrations were determined using the BCA standard protocol followed by the standard western immunoblotting protocol of proteins. The blots were developed using chemiluminescent substrate ECL (Thermo Fisher) and quantified using ImageJ software.

m^{6}A immunoprecipitation and sequencing—To profile the m^{6}A methylome, m^{6}A MeRIP-seq (Methylated RNA Immunoprecipitation Sequencing) was utilized.[11] 1 μg of mRNAs were isolated from total RNA using a Dynabeads mRNA DIRECT purification kit (Thermo Fisher). Then, mRNA was adjusted to about 10 ng μl^{-1} in 100 μl and fragmented using a Bioruptor ultrasonicator (Diagenode) with 30 s on/off for 30 cycles. After that, 5 ul of each sample is saved as the 'input'. m^{6}A immunoprecipitation (m^{6}A-IP) and library preparation were performed using the EpiMark N6-Methyladenosine enrichment kit (NEB). Input and RNA eluted from m^{6}A-IP were used to generate the library using a TruSeq-stranded mRNA sample preparation kit (Illumina). All sequencing was performed on an Illumina HiSeq 6000 according to the manufacturer's instructions.

Differential expression analysis for RNA-seq—As reported previously,[14] the input library of m^{6}A sequencing is essentially an mRNA sequencing library. Thus, we performed gene level differential expression analysis using the input libraries. Raw reads were trimmed using Cutadapt (4.2) and aligned to the hg38 genome (GRCh38.107) and mm10 (GRCm38.102) using HISAT2 (2.2.1)[62] and SAMtools (1.16.1). Aligned sequencing reads were analyzed using RADAR (0.2.4).[63] Then we perform differential methylation analysis of count data using the R package DESeq2 (1.36.0).[64] For both iBAT and hBAT samples, we used a cut-off P-value < 0.01 to select differential genes for pathway and gene ontology enrichment analyses. ConsensusPathDB and the "Metascape" online tool were used to perform enrichment analysis.

Differential methylation analysis for m^{6}A-seq—Using the R package RADAR,[63] approximately 25 million single-end 100-bp reads were generated for each sample. Counts

were normalized for library size and IP counts were adjusted for expression level by the gene-level read counts of input libraries. Bins with average IP-adjusted counts lower than 10 in both control and $M14^{KO}$ groups were removed. Then bins that were not enriched in IP were also filtered out. To consider the pairing of m^6A IP and input, we use the normalized, expression-level-(i.e. input)-adjusted and low-read-count-filtered IP counts. Using Wald tests, we tested for significant effects of $M14^{KO}$ on the m^6A enrichment/depletion. We adjusted for multiple testing using the Benjamini-Hochberg false discovery rate (FDR) controlling procedure.

H&E staining and immunohistochemistry staining—For Hematoxylin and Eosin (H&E) staining, the tissues of mice were fixed in 4% paraformaldehyde (PFA) overnight at 4 °C, followed by dehydration in 70% ethanol. After dehydration, tissues were embedded in paraffin. Multiple 5 μm sections were prepared and stained with H&E following the standard protocol. Images were acquired using a Zeiss AxioImager M1 (Carl Zeiss).
For immunostaining, paraffin-embedded tissues were deparaffinized twice in xylene and subsequently rehydrated. After heat-induced epitope retrieval using target retrieval solution (Dako), the tissues were blocked in PBS containing 10% goat serum with 0.1% Tween 20 for 60 min. After washing in PBS, slides from iBAT or iWAT tissues were incubated with various primary antibodies: rabbit anti-UCP1 (ab23841, Abcam, 1:250), antibody overnight at 4 °C. The next day, slides were washed in PBS and incubated with goat anti-rabbit immunoglobulin G (IgG) (H + L) secondary antibody conjugated with Alexa Fluor 594 (Invitrogen, 1:200). Slides from eWAT were incubated with anti-F4/80 (ab300421, Abcam, 1:5000) for 30min at room temperature, followed by secondary antibody is LeicaDS9800 (Bond Polymer Refine Detection). Nuclei were stained using DAPI (4′,6-diamidino-2-phenylindole).

Oil red O staining—Differentiated hBAT cells were washed twice with PBS and fixed with 10% buffered formalin for 30 minutes at room temperature. Cells were then stained with a filtered Oil Red O solution (0.5% Oil Red O in isopropyl alcohol) for 2 hours at room temperature. Cells were washed several times with distilled water for final visualization.

Measurement of blood parameters—Insulin (Crystal Chem #90082), Adiponectin (Crystal Chem #80569), and Leptin (Crystal Chem # 90030) were measured by ELISA kits according to the manufacturer's instructions.

PGE2 and PGF2a measurements—PGE2 and PGF2a concentrations were measured using the Prostaglandin E2 Express ELISA Kit and Prostaglandin F2a ELISA Kit, respectively (Cayman Chemical, Ann Arbor, MI) according to the manufacturer's instructions.

***In vitro* glucose uptake assays—**HepG2 cells, C2C12 cells, hWAT preadipocytes, and hBAT preadipocytes were seeded in a 96-well plate, cultured, and differentiated as described above. Cells were pretreated with the indicated antagonist for 1hr before treatment with 10 nM of PGF2a or 100 nM PGE2 overnight before glucose uptake was measured by Glucose Uptake-Glo Assay kit (Promega) according to the manufacturer's instructions.

Untargeted LS-MS/MS signaling lipidomics—For lipidomic profiling, control and $M14^{KO}$ mice were fasted overnight. Plasma, iBAT, and iBAT conditioned-Krebs solution were collected (left panel in Figure 3A). Global lipidomics were also performed on cell pellets and cell-conditioned medium of sgNTC-and sgM14-hBAT cells (right panel in Figure 3A). The details of Lipidomic profiling were provided previously.[7,9] For mouse samples, we performed moderated t-tests to discover lipids that were differentially abundant between $M14^{KO}$ and control samples, with the adjustment of covariates age, body weight, and litter.

QUANTIFICATION AND STATISTICAL ANALYSIS

Data is displayed as means ± S.E.M. and P-values were calculated using either two-tailed Student's t-test, or two-way ANOVA. All utilized statistical tests and 'n' numbers are presented in figure legends. For *in vitro* assays, 'n' corresponds to the number of experimental replicates. For animal assays or animal tissue extractions, 'n' corresponds to the number of mice used per genotype or condition. For human brown adipose tissue and plasma samples, 'n' corresponds to the number of donors used per group.

Figures have been generated using GraphPad Prism9, and BioRender.com.

Supplementary Material

Refer to Web version on PubMed Central for supplementary material.

ACKNOWLEDGMENTS

The authors thank Joslin Animal Physiology Core (P30 DK36836) and Bioinformatics Core. We would like to thank Stephane Gesta PhD, Michael Kiebish PhD, and Valerie Bussberg (BERG) for technical assistance with untargeted lipidomics. This work is supported by NIH grants RC2 DK139552 (R.N.K. and C.H.), R01 DK67536 (R.N.K.), UC4 DK116278 (R.N.K. and C.H.), and RM1 HG008935 (C.H.). R.N.K. acknowledges support from the Diabetes Research and Wellness Foundation Endowed Chair, and C.H. is a Howard Hughes Medical Institute Investigator. D.F.D.J. acknowledges support by Mary K. Iacocca Junior Postdoctoral Fellowship, American Diabetes Association grant #7–21-PDF-140, and NIH K99 DK135927. T.T. acknowledges support from the SUNSTAR Research Fellowship (Hiroo Kaneda Scholarship, Japan), the American Heart Association (grant 903968), and the Eleanor and Miles Shore Program Award from Harvard Medical School. Human Cohort 2: Kuopio Obesity Surgery Study (PI: J.P.) was supported by the Finnish Diabetes Research Foundation, Kuopio University Hospital project grant (EVO/VTR grants 2005–2021), the Academy of Finland grant (contract no. 138006), and the Finnish Cultural Foundation. Human Cohort 3: STOP DIABETES—From Knowledge to Solutions project was funded by the Strategic Research Council at the Academy of Finland in 2016–2019 (303537) and by the Academy of Finland 2020–2023 (332465), by the Novo Nordisk Foundation 2018–2020 (33980 and 63753), and by the Finnish Diabetes Research Foundation.

REFERENCES

1. Ouellet V, Labbé SM, Blondin DP, Phoenix S, Guérin B, Haman F, Turcotte EE, Richard D, and Carpentier AC (2012). Brown adipose tissue oxidative metabolism contributes to energy expenditure during acute cold exposure in humans. J. Clin. Invest 122, 545–552. 10.1172/JCI60433. [PubMed: 22269323]
2. Yoneshiro T, Aita S, Matsushita M, Kayahara T, Kameya T, Kawai Y, Iwanaga T, and Saito M (2013). Recruited brown adipose tissue as an antiobesity agent in humans. J. Clin. Invest 123, 3404–3408. 10.1172/JCI67803. [PubMed: 23867622]
3. Becher T, Palanisamy S, Kramer DJ, Eljalby M, Marx SJ, Wibmer AG, Butler SD, Jiang CS, Vaughan R, Schöder H, et al. (2021). Brown adipose tissue is associated with cardiometabolic health. Nat. Med 27, 58–65. 10.1038/s41591-020-1126-7. [PubMed: 33398160]

4. Shamsi F, Wang CH, and Tseng YH (2021). The evolving view of thermogenic adipocytes - ontogeny, niche and function. Nat. Rev. Endocrinol 17, 726–744. 10.1038/s41574-021-00562-6. [PubMed: 34625737]
5. Cypess AM (2022). Reassessing human adipose tissue. N. Engl. J. Med 386, 768–779. 10.1056/NEJMra2032804. [PubMed: 35196429]
6. Cao H, Gerhold K, Mayers JR, Wiest MM, Watkins SM, and Hotamisligil GS (2008). Identification of a lipokine, a lipid hormone linking adipose tissue to systemic metabolism. Cell 134, 933–944. 10.1016/j.cell.2008.07.048. [PubMed: 18805087]
7. Lynes MD, Leiria LO, Lundh M, Bartelt A, Shamsi F, Huang TL, Takahashi H, Hirshman MF, Schlein C, Lee A, et al. (2017). The cold-induced lipokine 12,13-diHOME promotes fatty acid transport into brown adipose tissue. Nat. Med 23, 631–637. 10.1038/nm.4297. [PubMed: 28346411]
8. Stanford KI, Lynes MD, Takahashi H, Baer LA, Arts PJ, May FJ, Lehnig AC, Middelbeek RJW, Richard JJ, So K, et al. (2018). 12,13-diHOME: an exercise-induced lipokine that increases skeletal muscle fatty acid uptake. Cell Metab. 27, 1111–1120.e3. 10.1016/j.cmet.2018.03.020. [PubMed: 29719226]
9. Leiria LO, Wang CH, Lynes MD, Yang K, Shamsi F, Sato M, Sugimoto S, Chen EY, Bussberg V, Narain NR, et al. (2019). 12-lipoxygenase regulates cold adaptation and glucose metabolism by producing the omega-3 lipid 12-HEPE from brown fat. Cell Metab. 30, 768–783.e7. 10.1016/j.cmet.2019.07.001. [PubMed: 31353262]
10. Sugimoto S, Mena HA, Sansbury BE, Kobayashi S, Tsuji T, Wang CH, Yin X, Huang TL, Kusuyama J, Kodani SD, et al. (2022). Brown adipose tissue-derived MaR2 contributes to cold-induced resolution of inflammation. Nat. Metab 4, 775–790. 10.1038/s42255-022-00590-0. [PubMed: 35760872]
11. Wang X, Lu Z, Gomez A, Hon GC, Yue Y, Han D, Fu Y, Parisien M, Dai Q, Jia G, et al. (2014). N6-methyladenosine-dependent regulation of messenger RNA stability. Nature 505, 117–120. 10.1038/nature12730. [PubMed: 24284625]
12. Liu J, Yue Y, Han D, Wang X, Fu Y, Zhang L, Jia G, Yu M, Lu Z, Deng X, et al. (2014). A METTL3-METTL14 complex mediates mammalian nuclear RNA N6-adenosine methylation. Nat. Chem. Biol 10, 93–95. 10.1038/nchembio.1432. [PubMed: 24316715]
13. Shi H, Wang X, Lu Z, Zhao BS, Ma H, Hsu PJ, Liu C, and He C (2017). YTHDF3 facilitates translation and decay of N(6)-methyladenosine-modified RNA. Cell Res. 27, 315–328. 10.1038/cr.2017.15. [PubMed: 28106072]
14. De Jesus DF, Zhang Z, Kahraman S, Brown NK, Chen M, Hu J, Gupta MK, He C, and Kulkarni RN (2019). m(6)A mRNA methylation regulates human β-cell biology in physiological states and in type 2 diabetes. Nat. Metab 1, 765–774. 10.1038/s42255-019-0089-9. [PubMed: 31867565]
15. Kahraman S, De Jesus DF, Wei J, Brown NK, Zou Z, Hu J, He C, and Kulkarni RN (2023). m 6 A mRNA methylation regulates early pancreatic β-cell differentiation. Preprint at bioRxiv. 10.1101/2023.08.03.551675.
16. F De Jesus D, Zhang Z, Brown NK, Li X, Xiao L, Hu J, Gaffrey MJ, Fogarty G, Kahraman S, Wei J, et al. (2024). Redox regulation of m6A methyltransferase METTL3 in b-cells controls the innate immune response in type 1 diabetes. Nat. Cell Biol 26, 421–437. 10.1038/s41556-024-01368-0. [PubMed: 38409327]
17. Wang Y, Gao M, Zhu F, Li X, Yang Y, Yan Q, Jia L, Xie L, and Chen Z (2020). METTL3 is essential for postnatal development of brown adipose tissue and energy expenditure in mice. Nat. Commun 11, 1648. 10.1038/s41467-020-15488-2. [PubMed: 32245957]
18. Claussnitzer M, Dankel SN, Kim KH, Quon G, Meuleman W, Haugen C, Glunk V, Sousa IS, Beaudry JL, Puviindran V, et al. (2015). FTO obesity variant circuitry and adipocyte browning in humans. N. Engl. J. Med 373, 895–907. 10.1056/NEJMoa1502214. [PubMed: 26287746]
19. Yan S, Zhou X, Wu C, Gao Y, Qian Y, Hou J, Xie R, Han B, Chen Z, Wei S, and Gao X (2023). Adipocyte YTH N(6)-methyladenosine RNA-binding protein 1 protects against obesity by promoting white adipose tissue beiging in male mice. Nat. Commun 14, 1379. 10.1038/s41467-023-37100-z. [PubMed: 36914671]
20. Coleman DL (1978). Obese and diabetes: two mutant genes causing diabetes-obesity syndromes in mice. Diabetologia 14, 141–148. 10.1007/BF00429772. [PubMed: 350680]

21. Michael MD, Kulkarni RN, Postic C, Previs SF, Shulman GI, Magnuson MA, and Kahn CR (2000). Loss of insulin signaling in hepatocytes leads to severe insulin resistance and progressive hepatic dysfunction. Mol. Cell 6, 87–97. 10.1016/S1097-2765(05)00015-8. [PubMed: 10949030]
22. Kong X, Banks A, Liu T, Kazak L, Rao RR, Cohen P, Wang X, Yu S, Lo JC, Tseng YH, et al. (2014). IRF4 is a key thermogenic transcriptional partner of PGC-1a. Cell 158, 69–83. 10.1016/j.cell.2014.04.049. [PubMed: 24995979]
23. Ricciotti E, and FitzGerald GA (2011). Prostaglandins and inflammation. Arterioscler. Thromb. Vasc. Biol 31, 986–1000. 10.1161/ATVBAHA.110.207449. [PubMed: 21508345]
24. Burkett JB, Doran AC, and Gannon M (2023). Harnessing prostaglandin E(2) signaling to ameliorate autoimmunity. Trends Immunol. 44, 162–171. 10.1016/j.it.2023.01.004. [PubMed: 36707339]
25. Woodward DF, Jones RL, and Narumiya S (2011). International union of basic and clinical pharmacology. LXXXIII: classification of prostanoid receptors, updating 15 years of progress. Pharmacol. Rev 63, 471–538. 10.1124/pr.110.003517. [PubMed: 21752876]
26. Watanabe K, Kawamori T, Nakatsugi S, Ohta T, Ohuchida S, Yamamoto H, Maruyama T, Kondo K, Ushikubi F, Narumiya S, et al. (1999). Role of the prostaglandin E receptor subtype EP1 in colon carcinogenesis. Cancer Res. 59, 5093–5096. [PubMed: 10537280]
27. af Forselles KJ, Root J, Clarke T, Davey D, Aughton K, Dack K, and Pullen N (2011). In vitro and in vivo characterization of PF-04418948, a novel, potent and selective prostaglandin EP_2 receptor antagonist. Br. J. Pharmacol 164, 1847–1856. 10.1111/j.1476-5381.2011.01495.x. [PubMed: 21595651]
28. Juteau H, Gareau Y, Labelle M, Sturino CF, Sawyer N, Tremblay N, Lamontagne S, Carrière MC, Denis D, and Metters KM (2001). Structure-activity relationship of cinnamic acylsulfonamide analogues on the human EP3 prostanoid receptor. Bioorg. Med. Chem 9, 1977–1984. 10.1016/s0968-0896(01)00110-9. [PubMed: 11504634]
29. Brittain RT, Boutal L, Carter MC, Coleman RA, Collington EW, Geisow HP, Hallett P, Hornby EJ, Humphrey PP, and Jack D (1985). AH23848: a thromboxane receptor-blocking drug that can clarify the pathophysiologic role of thromboxane A2. Circulation 72, 1208–1218. 10.1161/01.cir.72.6.1208. [PubMed: 2998642]
30. Pohl O, Marchand L, Gotteland JP, Coates S, Täubel J, and Lorch U (2018). Pharmacokinetics, safety and tolerability of OBE022, a selective prostaglandin F2a receptor antagonist tocolytic: A first-in-human trial in healthy postmenopausal women. Br. J. Clin. Pharmacol 84, 1839–1855. 10.1111/bcp.13622. [PubMed: 29708281]
31. Seely BL, Staubs PA, Reichart DR, Berhanu P, Milarski KL, Saltiel AR, Kusari J, and Olefsky JM (1996). Protein tyrosine phosphatase 1B interacts with the activated insulin receptor. Diabetes 45, 1379– 1385. 10.2337/diab.45.10.1379. [PubMed: 8826975]
32. Taniguchi CM, Emanuelli B, and Kahn CR (2006). Critical nodes in signalling pathways: insights into insulin action. Nat. Rev. Mol. Cell Biol 7, 85–96. 10.1038/nrm1837. [PubMed: 16493415]
33. Virkamäki A, Ueki K, and Kahn CR (1999). Protein-protein interaction in insulin signaling and the molecular mechanisms of insulin resistance. J. Clin. Invest 103, 931–943. 10.1172/JCI6609. [PubMed: 10194465]
34. Cypess AM, Lehman S, Williams G, Tal I, Rodman D, Goldfine AB, Kuo FC, Palmer EL, Tseng YH, Doria A, et al. (2009). Identification and importance of brown adipose tissue in adult humans. N. Engl. J. Med 360, 1509–1517. 10.1056/NEJMoa0810780. [PubMed: 19357406]
35. De Jesus DF, Orime K, Kaminska D, Kimura T, Basile G, Wang CH, Haertle L, Riemens R, Brown NK, Hu J, et al. (2020). Parental metabolic syndrome epigenetically reprograms offspring hepatic lipid metabolism in mice. J. Clin. Invest 130, 2391–2407. 10.1172/JCI127502. [PubMed: 32250344]
36. Dominissini D, Moshitch-Moshkovitz S, Schwartz S, Salmon-Divon M, Ungar L, Osenberg S, Cesarkas K, Jacob-Hirsch J, Amariglio N, Kupiec M, et al. (2012). Topology of the human and mouse m6A RNA methylomes revealed by m6A-seq. Nature 485, 201–206. 10.1038/nature11112. [PubMed: 22575960]

37. Meyer KD, Saletore Y, Zumbo P, Elemento O, Mason CE, and Jaffrey SR (2012). Comprehensive analysis of mRNA methylation reveals enrichment in 3′ UTRs and near stop codons. Cell 149, 1635–1646. 10.1016/j.cell.2012.05.003. [PubMed: 22608085]
38. Chambers JM, Addiego A, Flores-Mireles AL, and Wingert RA (2020). Ppargc1a controls ciliated cell development by regulating prostaglandin biosynthesis. Cell Rep. 33, 108370. 10.1016/j.celrep.2020.108370.
39. Bogacka I, Bogacki M, Gaglewska M, Kurzynska A, and Wasielak M (2013). In vitro effect of peroxisome proliferator activated receptor (PPAR) ligands on prostaglandin E2 synthesis and secretion by porcine endometrium during the estrous cycle and early pregnancy. J. Physiol. Pharmacol 64, 47–54. [PubMed: 23568971]
40. Miura T, Nishinaka T, and Terada T (2008). Different functions between human monomeric carbonyl reductase 3 and carbonyl reductase 1. Mol. Cell. Biochem 315, 113–121. 10.1007/s11010-008-9794-5. [PubMed: 18493841]
41. van Marken Lichtenbelt WD, Vanhommerig JW, Smulders NM, Drossaerts JMAFL, Kemerink GJ, Bouvy ND, Schrauwen P, and Teule GJJ (2009). Cold-activated brown adipose tissue in healthy men. N. Engl. J. Med 360, 1500–1508. 10.1056/NEJMoa0808718. [PubMed: 19357405]
42. Czech MP (2020). Mechanisms of insulin resistance related to white, beige, and brown adipocytes. Mol. Metab 34, 27–42. 10.1016/j.molmet.2019.12.014. [PubMed: 32180558]
43. Wang GX, Zhao XY, Meng ZX, Kern M, Dietrich A, Chen Z, Cozacov Z, Zhou D, Okunade AL, Su X, et al. (2014). The brown fat-enriched secreted factor Nrg4 preserves metabolic homeostasis through attenuation of hepatic lipogenesis. Nat. Med 20, 1436–1443. 10.1038/nm.3713. [PubMed: 25401691]
44. Keipert S, Lutter D, Schroeder BO, Brandt D, Ståhlman M, Schwarzmayr T, Graf E, Fuchs H, de Angelis MH, Tschöp MH, et al. (2020). Endogenous FGF21-signaling controls paradoxical obesity resistance of UCP1-deficient mice. Nat. Commun 11, 624. 10.1038/s41467-019-14069-2. [PubMed: 32005798]
45. Shamsi F, Xue R, Huang TL, Lundh M, Liu Y, Leiria LO, Lynes MD, Kempf E, Wang CH, Sugimoto S, et al. (2020). FGF6 and FGF9 regulate UCP1 expression independent of brown adipogenesis. Nat. Commun 11, 1421. 10.1038/s41467-020-15055-9. [PubMed: 32184391]
46. Thomou T, Mori MA, Dreyfuss JM, Konishi M, Sakaguchi M, Wolfrum C, Rao TN, Winnay JN, Garcia-Martin R, Grinspoon SK, et al. (2017). Adipose-derived circulating miRNAs regulate gene expression in other tissues. Nature 542, 450–455. 10.1038/nature21365. [PubMed: 28199304]
47. Zhao H, Chen X, Hu G, Li C, Guo L, Zhang L, Sun F, Xia Y, Yan W, Cui Z, et al. (2022). Small extracellular vesicles from brown adipose tissue mediate exercise cardioprotection. Circ. Res 130, 1490–1506. 10.1161/CIRCRESAHA.121.320458. [PubMed: 35387487]
48. Crewe C, and Scherer PE (2022). Intercellular and interorgan crosstalk through adipocyte extracellular vesicles. Rev. Endocr. Metab. Disord 23, 61–69. 10.1007/s11154-020-09625-x. [PubMed: 33447986]
49. Sustarsic EG, Ma T, Lynes MD, Larsen M, Karavaeva I, Havelund JF, Nielsen CH, Jedrychowski MP, Moreno-Torres M, Lundh M, et al. (2018). Cardiolipin synthesis in brown and beige fat mitochondria is essential for systemic energy homeostasis. Cell Metab. 28, 159–174.e11. 10.1016/j.cmet.2018.05.003. [PubMed: 29861389]
50. Whitehead A, Krause FN, Moran A, MacCannell ADV, Scragg JL, McNally BD, Boateng E, Murfitt SA, Virtue S, Wright J, et al. (2021). Brown and beige adipose tissue regulate systemic metabolism through a metabolite interorgan signaling axis. Nat. Commun 12, 1905. 10.1038/s41467-021-22272-3. [PubMed: 33772024]
51. Feldmann HM, Golozoubova V, Cannon B, and Nedergaard J (2009). UCP1 ablation induces obesity and abolishes diet-induced thermogenesis in mice exempt from thermal stress by living at thermoneutrality. Cell Metab. 9, 203–209. 10.1016/j.cmet.2008.12.014. [PubMed: 19187776]
52. Kajimura S, and Spiegelman BM (2020). Confounding issues in the ‘humanized’BAT of mice. Nat. Metab 2, 303–304. 10.1038/s42255-020-0192-y. [PubMed: 32405619]
53. Vegiopoulos A, Müller-Decker K, Strzoda D, Schmitt I, Chichelnitskiy E, Ostertag A, Berriel Diaz M, Rozman J, Hrabe de Angelis M, Nüsing RM, et al. (2010). Cyclooxygenase-2 controls

energy homeostasis in mice by de novo recruitment of brown adipocytes. Science 328, 1158–1161. 10.1126/science.1186034. [PubMed: 20448152]

54. Abe I, Oguri Y, Verkerke ARP, Monteiro LB, Knuth CM, Auger C, Qiu Y, Westcott GP, Cinti S, Shinoda K, et al. (2022). Lipolysis-derived linoleic acid drives beige fat progenitor cell proliferation. Dev. Cell 57, 2623–2637.e8. 10.1016/j.devcel.2022.11.007. [PubMed: 36473459]
55. García-Alonso V, López-Vicario C, Titos E, Morán-Salvador E, González-Périz A, Rius B, Párrizas M, Werz O, Arroyo V, and Clària J (2013). Coordinate functional regulation between microsomal prostaglandin E synthase-1 (mPGES-1) and peroxisome proliferator-activated receptor γ (PPARγ) in the conversion of white-to-brown adipocytes. J. Biol. Chem 288, 28230–28242. 10.1074/jbc.M113.468603. [PubMed: 23943621]
56. García-Alonso V, and Clà ria J (2014). Prostaglandin E2 signals white-to-brown adipogenic differentiation. Adipocyte 3, 290–296. 10.4161/adip.29993. [PubMed: 26317053]
57. Gong R, Morris DJ, and Brem AS (2008). Human renal 11beta-hydroxysteroid dehydrogenase 1 functions and co-localizes with COX-2. Life Sci. 82, 631–637. 10.1016/j.lfs.2007.12.019. [PubMed: 18261751]
58. Kang Q, Zhu X, Ren D, Ky A, MacDougald OA, O'Rourke RW, and Rui L (2023). Adipose METTL14-elicited N6-methyladenosine promotes obesity, insulin resistance, and NAFLD through suppressing b adrenergic signaling and lipolysis. Adv. Sci. (Weinh) 10, e2301645. 10.1002/advs.202301645.
59. Halali F, Lapveteläinen A, Aittola K, Männikkö R, Tilles-Tirkkonen T, Järvelä-Reijonen E, Absetz P, Kolehmainen M, Schwab U, Lindströ m J, et al. (2022). Associations between weight loss history and factors related to type 2 diabetes risk in the Stop Diabetes study. Int. J. Obes. (Lond) 46, 935–942. 10.1038/s41366-021-01061-4. [PubMed: 35022546]
60. Xue R, Lynes MD, Dreyfuss JM, Shamsi F, Schulz TJ, Zhang H, Huang TL, Townsend KL, Li Y, Takahashi H, et al. (2015). Clonal analyses and gene profiling identify genetic biomarkers of the thermogenic potential of human brown and white preadipocytes. Nat. Med 21, 760–768. 10.1038/nm.3881. [PubMed: 26076036]
61. Tsuji T, Zhang Y, and Tseng YH (2023). Generation of brown fat-specific knockout mice using a combined Cre-LoxP, CRISPR-Cas9, and adeno-associated virus single-guide RNA system. J. Vis. Exp 193. 10.3791/65083.
62. Kim D, Langmead B, and Salzberg SL (2015). HISAT: a fast spliced aligner with low memory requirements. Nat. Methods 12, 357–360. 10.1038/nmeth.3317. [PubMed: 25751142]
63. Zhang Z, Zhan Q, Eckert M, Zhu A, Chryplewicz A, De Jesus DF, Ren D, Kulkarni RN, Lengyel E, He C, and Chen M (2019). RADAR: differential analysis of MeRIP-seq data with a random effect model. Genome Biol. 20, 294. 10.1186/s13059-019-1915-9. [PubMed: 31870409]
64. Love MI, Huber W, and Anders S (2014). Moderated estimation of fold change and dispersion for RNA-seq data with DESeq2. Genome Biol. 15, 550. 10.1186/s13059-014-0550-8. [PubMed: 25516281]

Highlights

- *METTL14*-deficient BAT improves insulin sensitivity via interorgan communication
- PGE2 and PGF2a are BAT-secreted insulin sensitizers and iWAT-browning inducers
- PGE2 and PGF2a improve insulin sensitivity via an AKT-dependent axis
- *METTL14* deficiency increases *PTGES2* and *CBR1* mRNA stability

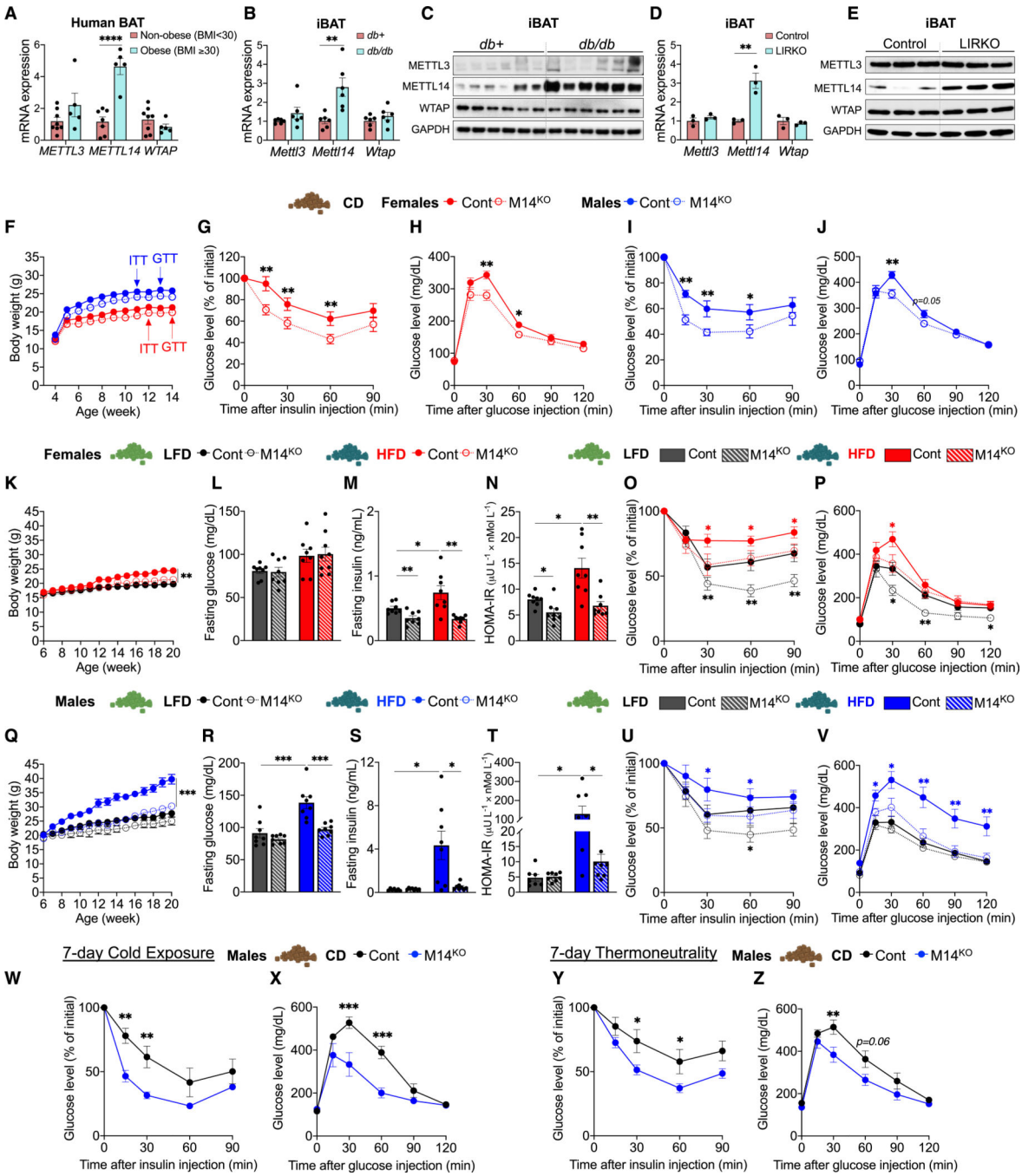

Figure 1. Ablation of *Mettl14* in BAT improves systemic insulin sensitivity and glucose tolerance in mice

(A) RT-qPCR of m^{6}A writer genes *METTL3*, *METTL14*, and *WTAP* in human brown adipose tissues (n = 8 for non-obese; n = 5 for obese).

(B) RT-qPCR of *Mettl3*, *Mettl14*, and *Wtap* in interscapular brown adipose tissues of control (*db/+*) and *db/db* mice (n = 6/group).

(C) Western blots of METTL3, METTL14, WTAP, and GAPDH in interscapular brown adipose tissues of control (*db/+*) and *db/db* mice (n = 6/group).

(D) RT-qPCR of *Mettl3*, *Mettl14*, and *Wtap* in interscapular brown adipose tissues of control and LIRKO mice (n = 3/group).
(E) Western blots of METTL14 and GAPDH in interscapular brown adipose tissues of control and LIRKO mice (n = 3/group).
(F) Body weight trajectories of CD-fed mice (females, n = 12 for control and n = 9 for $M14^{KO}$ groups; males, n = 10 for each control and $M14^{KO}$ group).
(G and H) Intraperitoneal insulin tolerance tests (G) and intraperitoneal glucose tolerance tests (H) of CD-fed females (ITT, n = 12 for control and n = 9 for $M14^{KO}$ groups; GTT, n = 10 for control and n = 9 for $M14^{KO}$ groups).
(I and J) Intraperitoneal insulin tolerance tests (I) and intraperitoneal glucose tolerance tests (J) of CD-fed males (ITT, n = 9 for control and n = 6 for $M14^{KO}$ groups; GTT, n = 8 for control and n = 7 for $M14^{KO}$ groups).
(K and Q) Body weight trajectories of LFD- or HFD-fed control and $M14^{KO}$ females (K) and males (Q) (females, n = 8 for control and n = 5 for $M14^{KO}$ groups on LFD, n = 8 for control and n = 6 for $M14^{KO}$ groups on HFD; males, n = 8 each for control and $M14^{KO}$ groups on LFD or HFD).
(L and R) Fasting glucose levels of control and $M14^{KO}$ females (L) and males (R) (females, n = 8 for control and $M14^{KO}$ groups on LFD, n = 8 for control and n = 9 for $M14^{KO}$ groups on HFD; males, n = 8 for each group).
(M and S) Fasting insulin levels in the serum of control and $M14^{KO}$ females (M) and males (S) (females, n = 8 for each group; males, n = 7 for control and n = 8 for $M14^{KO}$ on LFD; n = 8 for each group on HFD).
(N and T) HOMA-IR of LFD- or HFD-fed control and $M14^{KO}$ females (N) and males (T) (females, n = 8 for each group; males, n = 7 for control and n = 8 for $M14^{KO}$ on LFD, n = 8 for each group on HFD).
(O and U) Intraperitoneal insulin tolerance tests of LFD- or HFD-fed control and $M14^{KO}$ females (O) and males (U) (females, n = 8 for control and n = 9 for $M14^{KO}$ on HFD, n = 8 for each group on LFD; males, n = 7 for each group on HFD, n = 8 for control, and n = 7 for $M14^{KO}$ on LFD).
(P and V) Intraperitoneal glucose tolerance tests of LFD- or HFD-fed control and $M14^{KO}$ females (P) and males (V) (females, n = 8 for control, n = 9 for $M14^{KO}$ on HFD, and n = 8 for each group on LFD; males, n = 8 for each group).
(W and X) Intraperitoneal insulin tolerance tests (W) and intraperitoneal glucose tolerance tests (X) of CD-fed control and $M14^{KO}$ males treated with 7-day cold exposure (n = 5 for the control group and n = 6 for $M14^{KO}$ group).
(Y and Z) Intraperitoneal insulin tolerance tests (Y) and intraperitoneal glucose tolerance tests (Z) of CD-fed control and $M14^{KO}$ males treated with 7-day thermoneutrality exposure (ITT, n = 7 for control and n = 9 for $M14^{KO}$ group; GTT, n = 5 for control and n = 6 for $M14^{KO}$ group).
All samples in each panel are biologically independent. Data are expressed as means ± SEM. *p < 0.05, **p < 0.01, and ***p < 0.001 by two-way ANOVA (F–K, O–Q, and U–Z) and two-tailed unpaired t test (A, B, D, L–N, and R–T).
See also Figure S1.

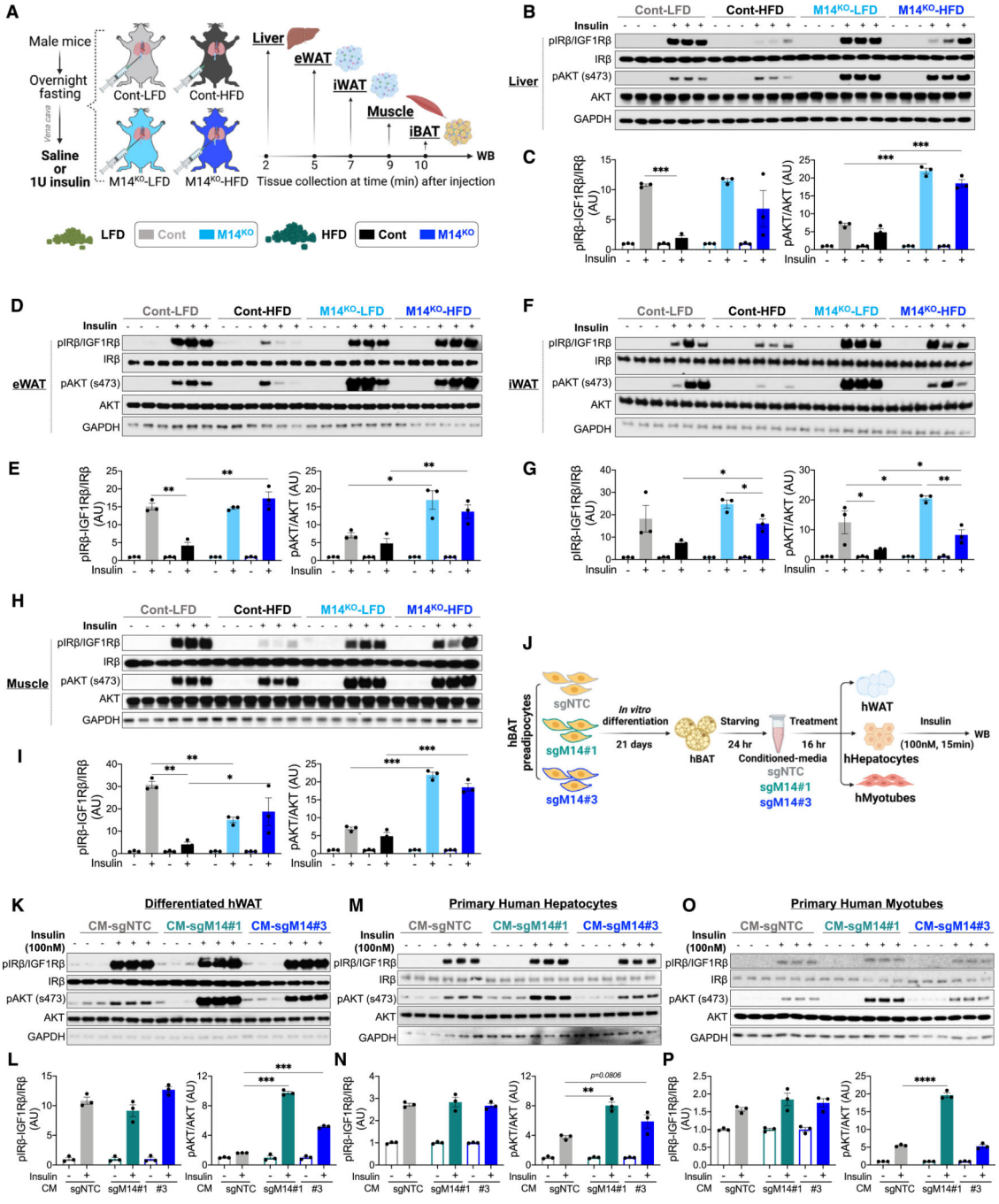

Figure 2. Ablation of *Mettl14* in BAT enhances insulin sensitivity of mouse peripheral metabolic tissues and human metabolic cells by secretory factors

(A) Schematic of metabolic tissue collection at indicated time points after *vena cava* saline/insulin injection in LFD- or HFD-fed control and $M14^{KO}$ male mice (n = 3/group).

(B–I) The insulin-stimulated pIRβ/IGF1Rβ and $pAKT_{s473}$ in the liver (B and C), eWAT (D and E), iWAT (F and G), and muscle (H and I) after injection of 1U insulin into the *vena cava* (n = 3/group).

(J) Experimental scheme of *in vitro* co-culture experiments. Differentiated human white adipocytes, human primary hepatocytes, and differentiated human myotubes were treated

with differentiated human brown adipocytes conditioned media for 16 h and stimulated with 100 nM insulin for 15 min.

(K–P) The insulin-stimulated pIRβ/IGF1Rβ and $pAKT_{s473}$ in human white adipocytes (K and L), human primary hepatocytes (M and N), and differentiated human myotubes (O and P) treated with or without hBAT-conditioned media ($n = 3$ independent experiments).

All samples in each panel are biologically independent. Data are expressed as means ± SEM. *$p < 0.05$, **$p < 0.01$, and ***$p < 0.001$ by two-tailed unpaired t test (B, E, G, I, L, N, and P).

CM, conditioned media.

See also Figure S2.

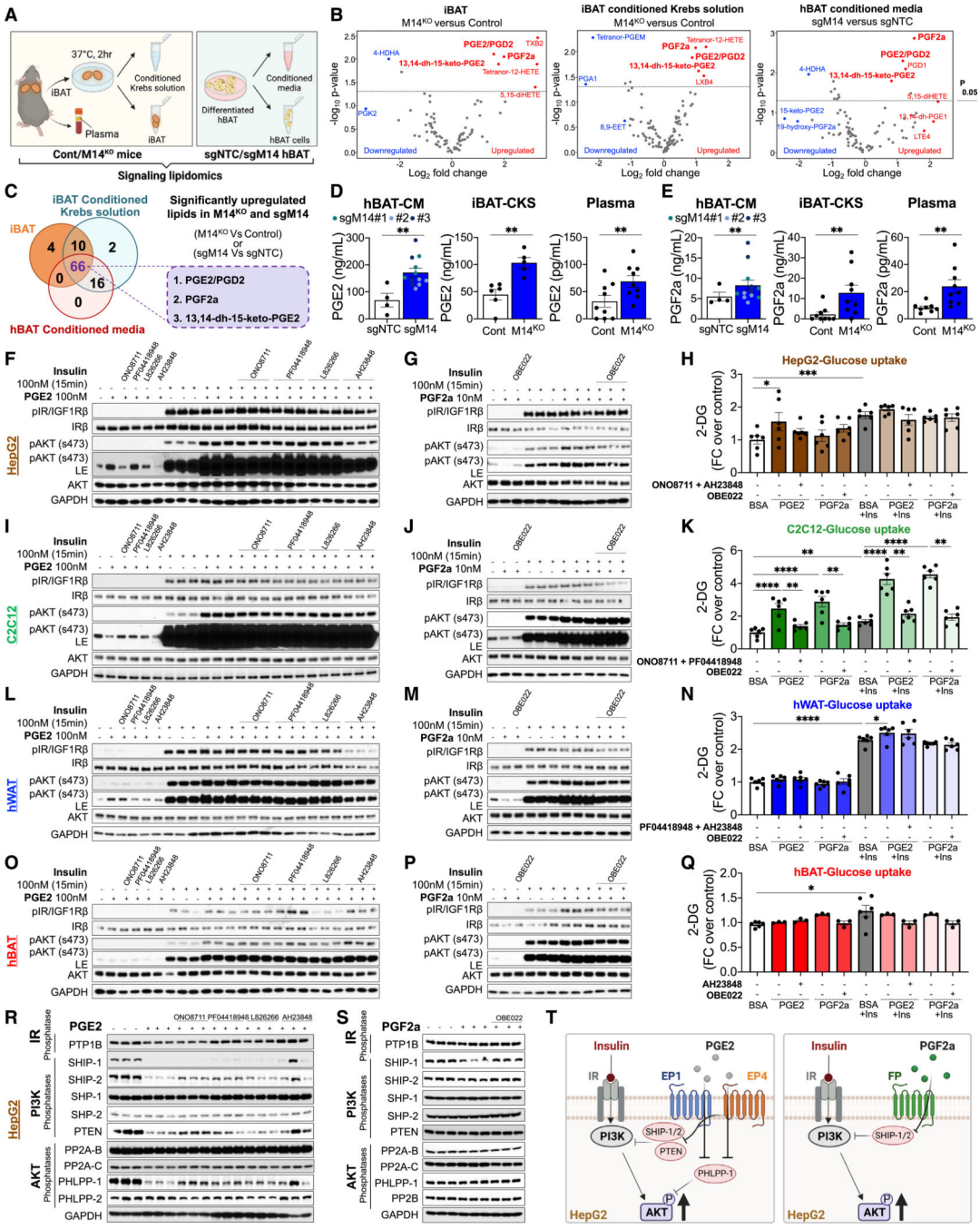

Figure 3. Ablation of *Mettl14* improves insulin sensitivity primarily through prostaglandin E2 and prostaglandin F2a

(A) Schematic of sample preparation for untargeted signaling lipidomics.

(B) Volcano plots of differentially downregulated (blue data points) and upregulated (red data points) lipids in M14^{KO}-iBAT, M14^{KO}-iBAT conditioned Krebs solution and sgM14-hBAT-conditioned media identified by LC-MS lipid analysis (n = 9 for iBAT and iBAT conditioned Krebs solution, n = 3–6 for hBAT-conditioned media, $\log_2$ [fold change] threshold = 2, p value threshold = 0.05).

(C) Venn diagram of all differentially abundant lipids in $M14^{KO}$-iBAT, $M14^{KO}$-iBAT conditioned Krebs solution, and sgM14-hBAT-conditioned media (n = 9 for iBAT and iBAT conditioned Krebs solution, n = 3–6 for hBAT-conditioned media, $\log_2$ [fold change] threshold = 2, p value threshold = 0.05).

(D and E) PGE2 (D) and PGF2a (E) concentrations in hBAT-conditioned media (CM), iBAT conditioned Krebs solution (CKS), and mouse plasma measured by ELISAs (hBAT-CM, n = 4 for sgNTC, n = 4 for sgM14#1/2/3; iBAT-CKS, n = 5–9/group; plasma, n = 9/group).

(F, I, L, and O) Western blot of pIRβ/IGF1Rβ and $pAKT_{s473}$ in HepG2 (F), C2C12 (I), hWAT (L), and hBAT (O) cells induced by PGE2 (100 nM) or insulin (100 nM) pretreated with EP1/2/3/4 receptor antagonists ONO8711, PF04418948, L826266, and AH23848 (LE, longer exposure; n = 3 biological replicates).

(G, J, M, and P) Western blot of represented pIRβ/IGF1Rβ and $pAKT_{s473}$ in HepG2 (G), C2C12 (J), hWAT (M), and hBAT (P) cells induced by PGF2a (10 nM) or insulin (100 nM) pre-treated with FP receptor antagonist OBE022 (LE, longer exposure; n = 3 biological replicates).

(H, K, N, and Q) 2-deoxyglucose uptake in HepG2 (H), C2C12 (K), hWAT (N), and hBAT (Q) cells pre-treated with PGE2 (100 nM for HepG2, C2C12, hWAT, and hBAT cells) or PGF2a (10 nM) and indicated antagonist(s) overnight, followed by treatment with insulin (100 nM) for 15 min (HepG2, n = 6 biological replicates; C2C12, n = 6 biological replicates; hWAT, n = 6 biological replicates; hBAT, n = 3–6 biological replicates).

(R and S) Western blot of phosphatases for IR, PI3K, and AKT in HepG2 cells pre-treated with PGE2 (R) or PGF2a (S) in the presence of indicated antagonists (n =3 biological replicates).

(T) Proposed model for mechanisms of action for PGE2 and PGF2a in HepG2 cells. Data are presented as mean ± SEM of biologically independent samples. *$p < 0.05$, **$p < 0.01$, and ***$p < 0.001$ by two-tailed unpaired t test (D, E, H, K, N, and Q).

See also Figures S3–S5 and Table S2.

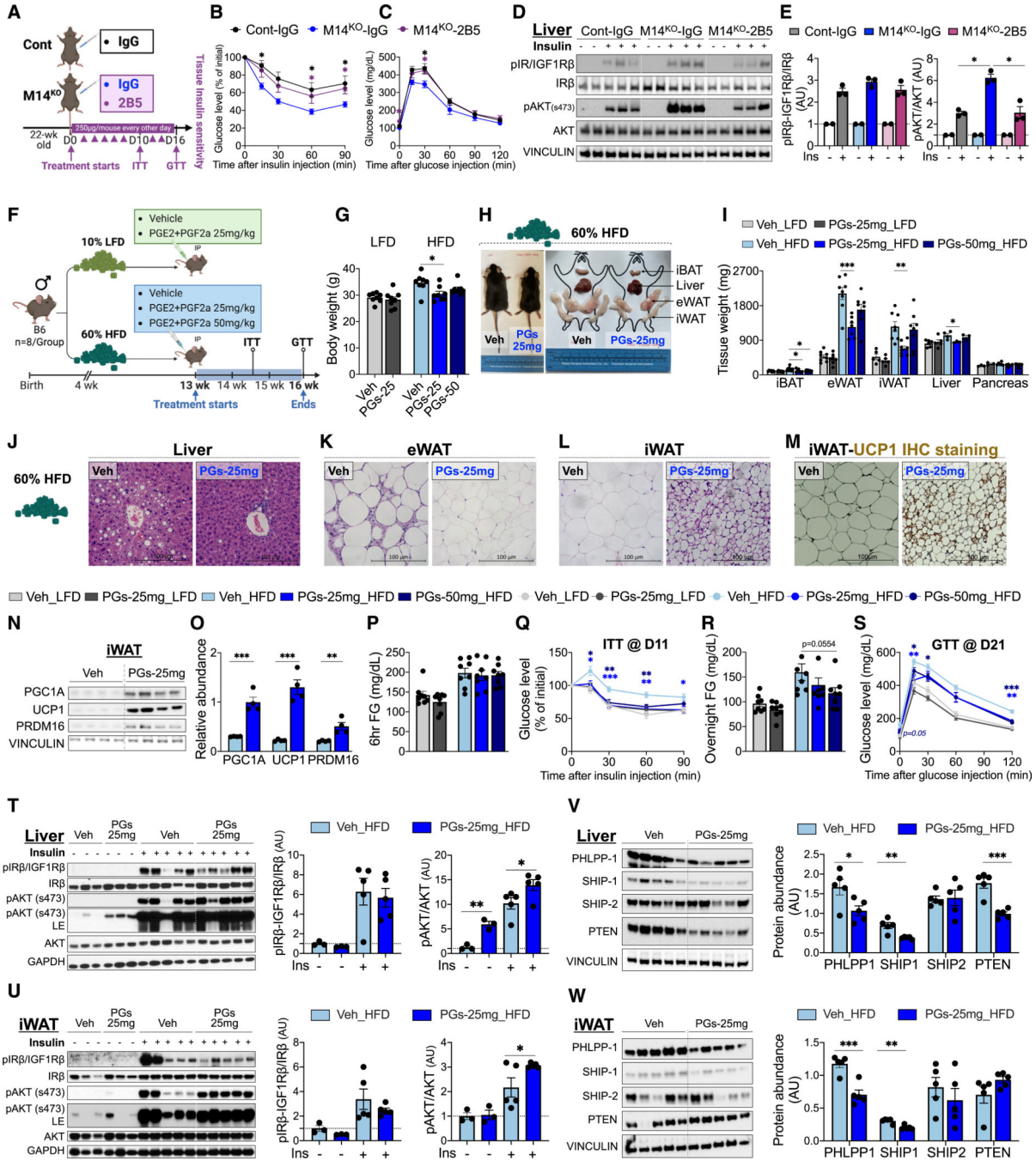

Figure 4. PGE2 and PGF2a are the M14^{KO}-iBAT secreted insulin sensitizers

(A) Schematic of neutralization experiments in control and M14^{KO} mice. Control mice were injected with isotype-matching IgG control, and M14^{KO} mice were injected with either IgG control antibody or 2B5 (anti-human PGE2 recombinant antibody).

(B and C) Intraperitoneal insulin tolerance tests (B) and intraperitoneal glucose tolerance tests (C) of control mice injected with IgG and M14^{KO} mice injected with IgG or 2B5 (ITT, n = 9 for the control and n = 6 for M14^{KO} groups; GTT, n = 6/group).

(D and E) Western blot (D) and quantification (E) of pIRβ/IGF1Rβ and $pAKT_{s473}$ in the liver from control or $M14^{KO}$ mice that received IgG or 2B5, followed by 1 U insulin injection via *vena cava* (n = 2 for non-stimulated group; n = 3 for insulin-stimulated group).
(F) Overview of the administration of PGE2+PGF2a every other day via intraperitoneal injections of either vehicle (saline), 25 mg/kg (12.5 mg/kg PGE2 + 12.5 mg/kg PGF2a), or 50 mg/kg (25 mg/kg PGE2 + 25 mg/kg PGF2a) PGE2+PGF2a into 12-week-old mice fed either with LFD or HFD for 21 days (n = 8/group).
(G) Body weight of the vehicle-, 25 mg/kg PGE2+PGF2a-, or 50 mg/kg PGE2+PGF2a-injected LFD- or HFD-fed mice after 3-week injection (n = 8/group).
(H) Representative gross appearance of body size, adipose tissues, and liver in vehicle- or 25 mg/kg PGE2+PGF2a-treated mice (n = 3).
(I) Tissue weight of iBAT, iWAT, eWAT, liver, and pancreas of vehicle-, 25 mg/kg PGE2+PGF2a-, or 50 mg/kg PGE2+PGF2a-injected LFD- or HFD-fed mice after 3-week injection (n = 3–8/group).
(J–M) Representative H&E staining in the liver (J), eWAT (K), iWAT (L), and UCP1 immunohistochemistry staining of iWAT (M) from vehicle- or 25 mg/kg PGE2+PGF2a-injected HFD-fed mice (n = 3).
(N and O) Western blot (N) and quantification (O) of PGC1α, UCP1, and PRDM16 in iWAT from vehicle- or 25 mg/kg PGE2+PGF2a-injected HFD-fed mice (n = 4/group).
(P–S) 6 h-fasting glucose levels (P), intraperitoneal insulin tolerance tests (Q), overnight-fasting glucose levels (R), and intraperitoneal glucose tolerance tests (S) of vehicle-, 25 mg/kg PGE2+PGF2a-, or 50 mg/kg PGE2+PGF2a-injected LFD- or HFD-fed mice (n = 8/group).
(T and U) Western blot and quantification of pIRβ/IGF1Rβ and $pAKT_{s473}$ in the liver (T) and iWAT (U) after 21-day injection of saline or 25 mg/kg PGE2+PGF2a, followed by 1 U insulin injection via *vena cava* (n = 3 for non-stimulated group; n = 5 for insulin-stimulated group).
(V and W) Western blot and quantification of indicated phosphatases in liver (V) and iWAT (W) (n = 5/group).
All samples in each panel are biologically independent. Data are expressed as means ± SEM. *$p < 0.05$, **$p < 0.01$, and ***$p < 0.001$ by two-tailed unpaired t test (O and T–W) and two-way ANOVA (B, C, E, G, I, and P–S).
See also Figure S6.

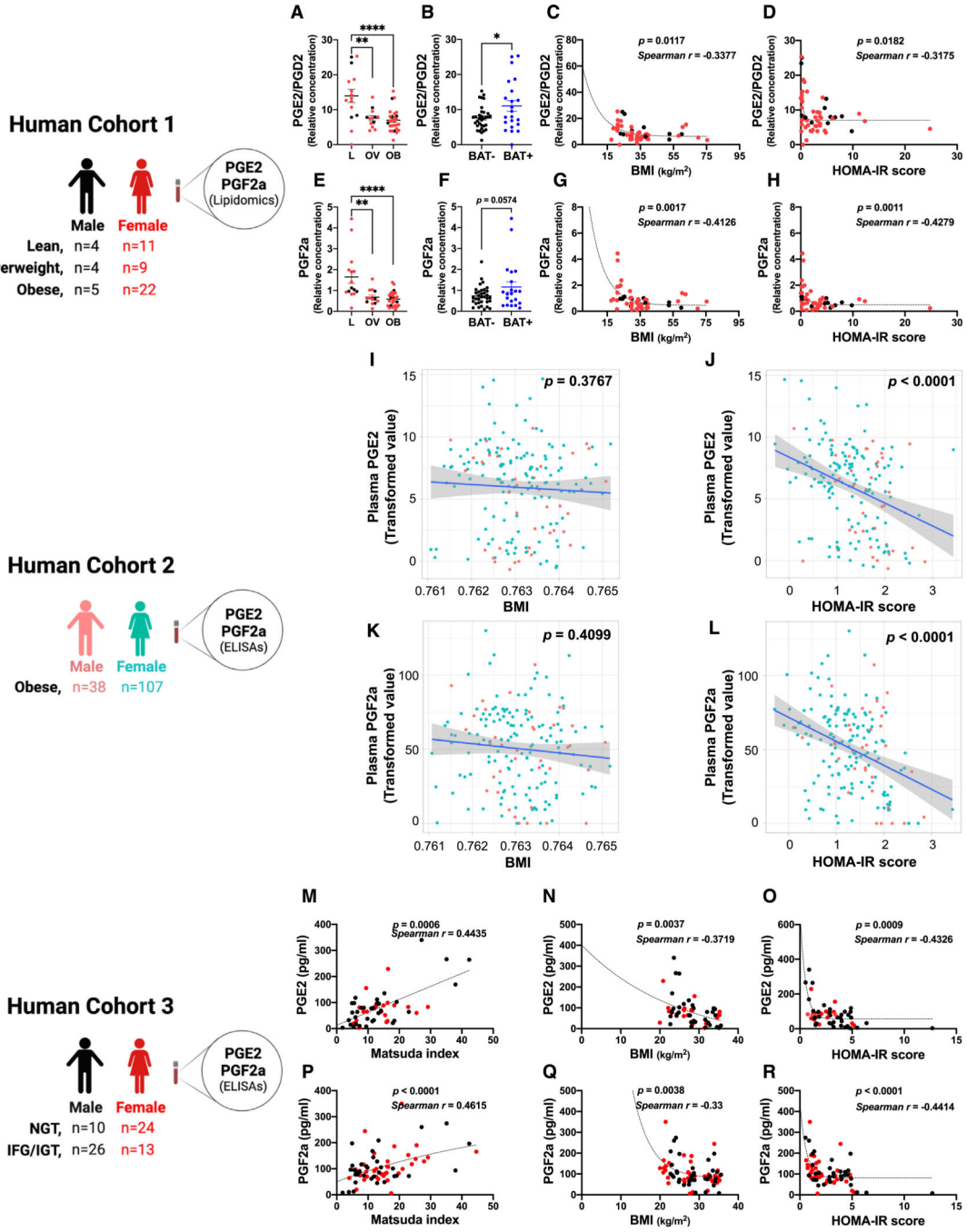

Figure 5. Plasma levels of PGE2 and PGF2a are negatively associated with obesity and insulin resistance in humans

(A) Plasma PGE2/PGD2 levels in lean (BMI < 25 kg/m^2), overweight (BMI > 25 kg/m^2, <30 kg/m^2), and obese (BMI > 30 kg/m^2) subjects (n = 55). **p < 0.01, ***p < 0.001. Data are represented as mean ± SEM. L, lean; OV, overweight; OB, obese (L, n = 15; OV, n = 13; OB, n = 27).

(B) Plasma levels of PGE2/PGD2 in individuals categorized as BAT— or BAT+ (BAT—, n = 33; BAT+, n = 22).

(C) Spearman correlation between the plasma levels of PGE2/PGD2 and BMI (n = 55).

(D) Spearman correlation between the plasma levels of PGE2/PGD2 and insulin resistance measured by HOMA-IR ($n = 55$).
(E) Plasma PGF2a levels in lean (BMI < 25 kg/m^2), overweight (BMI > 25 kg/m^2, <30 kg/m^2), and obese (BMI > 30 kg/m^2) subjects (L, $n = 15$; OV, $n = 13$; OB, $n = 27$).
(F) Plasma levels of PGF2a in individuals categorized as BAT— or BAT+ (BAT—, $n = 33$; BAT+, $n = 22$).
(G) Spearman correlation between the plasma levels of PGF2a and BMI ($n = 55$).
(H) Spearman correlation between the plasma levels of PGF2a and insulin resistance measured by HOMA-IR ($n = 55$).
(I) Correlation between serum PGE2 levels and BMI in individuals who are obese ($n = 175$).
(J) Correlation between serum PGF2a levels and insulin resistance measured by HOMA-IR in individuals who are obese ($n = 175$).
(K) Correlation between serum PGE2 levels and BMI in individuals who are obese ($n = 175$).
(L) Correlation between serum PGF2a levels and insulin resistance measured by HOMA-IR in individuals who are obese ($n = 175$).
(M) Spearman correlation between the plasma levels of PGE2 and Matsuda index ($n = 59$).
(N) Spearman correlation between the plasma levels of PGE2 and BMI ($n = 59$).
(O) Spearman correlation between the plasma levels of PGE2 and insulin resistance measured by HOMA-IR ($n = 59$).
(P) Spearman correlation between the plasma levels of PGF2a and Matsuda index ($n = 75$).
(Q) Spearman correlation between the plasma levels of PGF2a and BMI ($n = 75$).
(R) Spearman correlation between the plasma levels of PGF2a and insulin resistance measured by HOMA-IR ($n = 75$).
For human cohort 1, relative concentrations are used in (A)–(F) because the lipid quantification data were detected using non-targeted lipidomics.
For human cohort 2, PGE2 and PGF2a concentrations were measured by ELISAs. Transformed values of metabolites and clinical variables levels were used.
For human cohort 3, PGE2 and PGF2a levels were measured by ELISAs. Absolute concentrations were used.
All samples in each panel are biologically independent. *$p < 0.05$, **$p < 0.01$, ***$p < 0.001$. See also Figure S7 and Tables S3–S5.

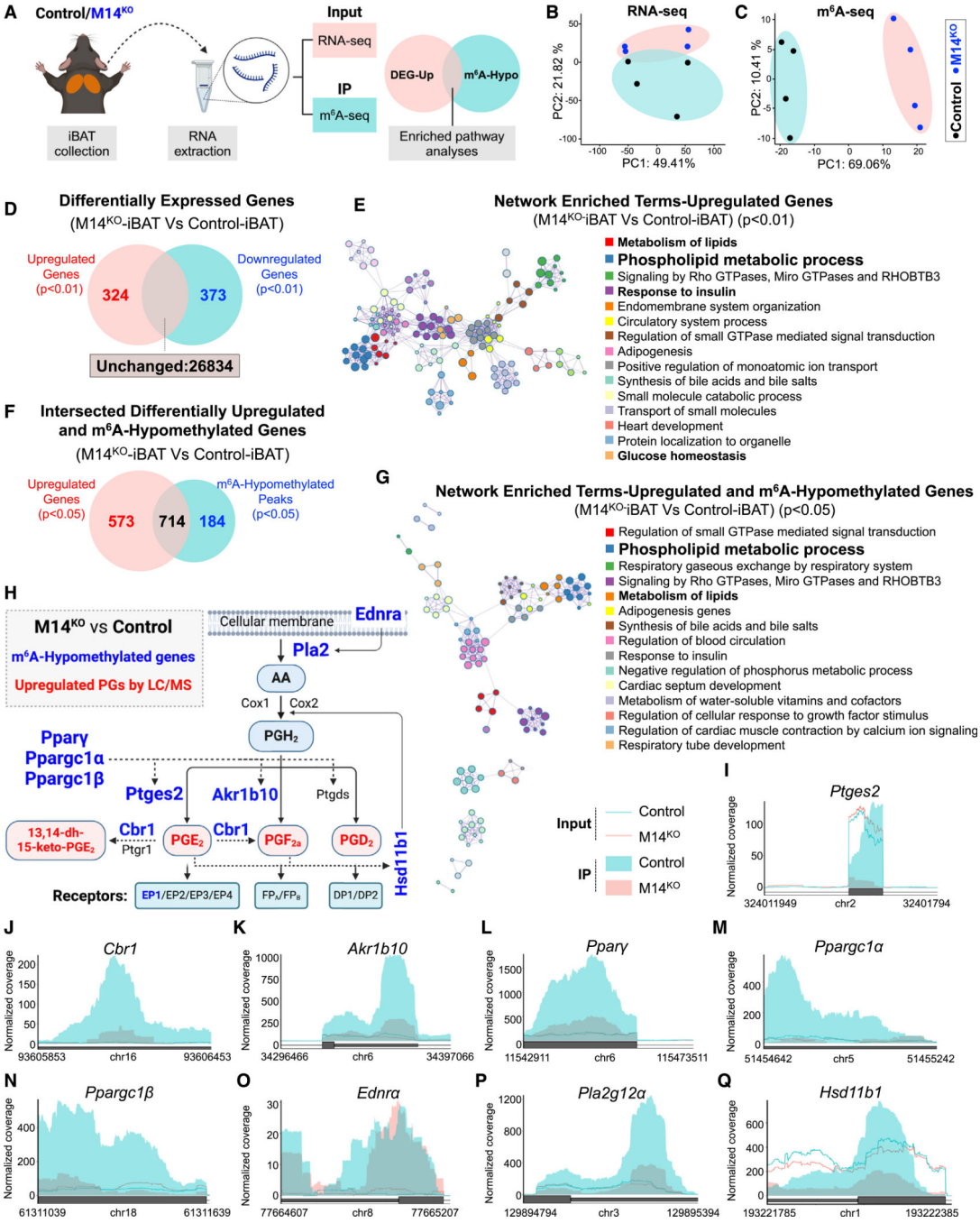

Figure 6. METTL14 selectively methylates transcripts encoding prostaglandin biosynthesis enzymes and their regulators

(A) Schematic illustration of the RNA-seq and m^{6}A-seq bioinformatic analyses strategy of iBAT samples from control and M14^{KO} mice.

(B) PCA plot of RNA-seq in controls (black dots, n = 4 independent biological samples) and M14^{KO}-iBAT (blue dots, n = 4 independent biological samples).

(C) PCA plot of m^{6}A-seq in controls (black dots, n = 4 independent biological samples) and M14^{KO}-iBAT (blue dots, n = 4 independent biological samples).

(D) Venn diagram representation of the upregulated (red), downregulated (blue), and unchanged genes (black) of $M14^{KO}$-iBAT compared with control-iBAT.
Statistical analyses were performed using the Benjamin-Hochberg procedure, and genes were filtered for $p < 0.01$.
(E) Top 15 enriched GOs and pathways of upregulated genes in $M14^{KO}$-iBAT versus control-iBAT.
(F) Venn diagram representation of the intersection between upregulated genes (red) with m^6A-hypomethylated genes (blue) in $M14^{KO}$-iBAT versus control-iBAT. Genes were filtered for $p < 0.05$.
(G) Functional enrichment of intersected genes in (F).
(H) Representation of prostaglandins biosynthesis pathway based on KEGG and Wikipathway annotations depicting several m^6A hypomethylated genes (blue) and unchanged genes (black) and the upregulated prostaglandins suggested by LC-MS/MS lipidomics (red) in $M14^{KO}$-iBAT versus control-iBAT (genes filtered for $p < 0.05$).
(I–Q) Coverage plots of m^6A peaks in *Ptges2* (I), *Cbr1* (J), *Akr1b10* (K), *Pparγ* (L), *Ppargc1α* (M), *Ppargc1β* (N), *Ednrα* (O), *Plasg12*a (P), and *Hsd11b1* (Q) transcripts in $M14^{KO}$-iBAT versus control-iBAT. Plotted coverages are the median of the *n* replicates presented.
All samples in each panel are biologically independent.
See also Figure S8.

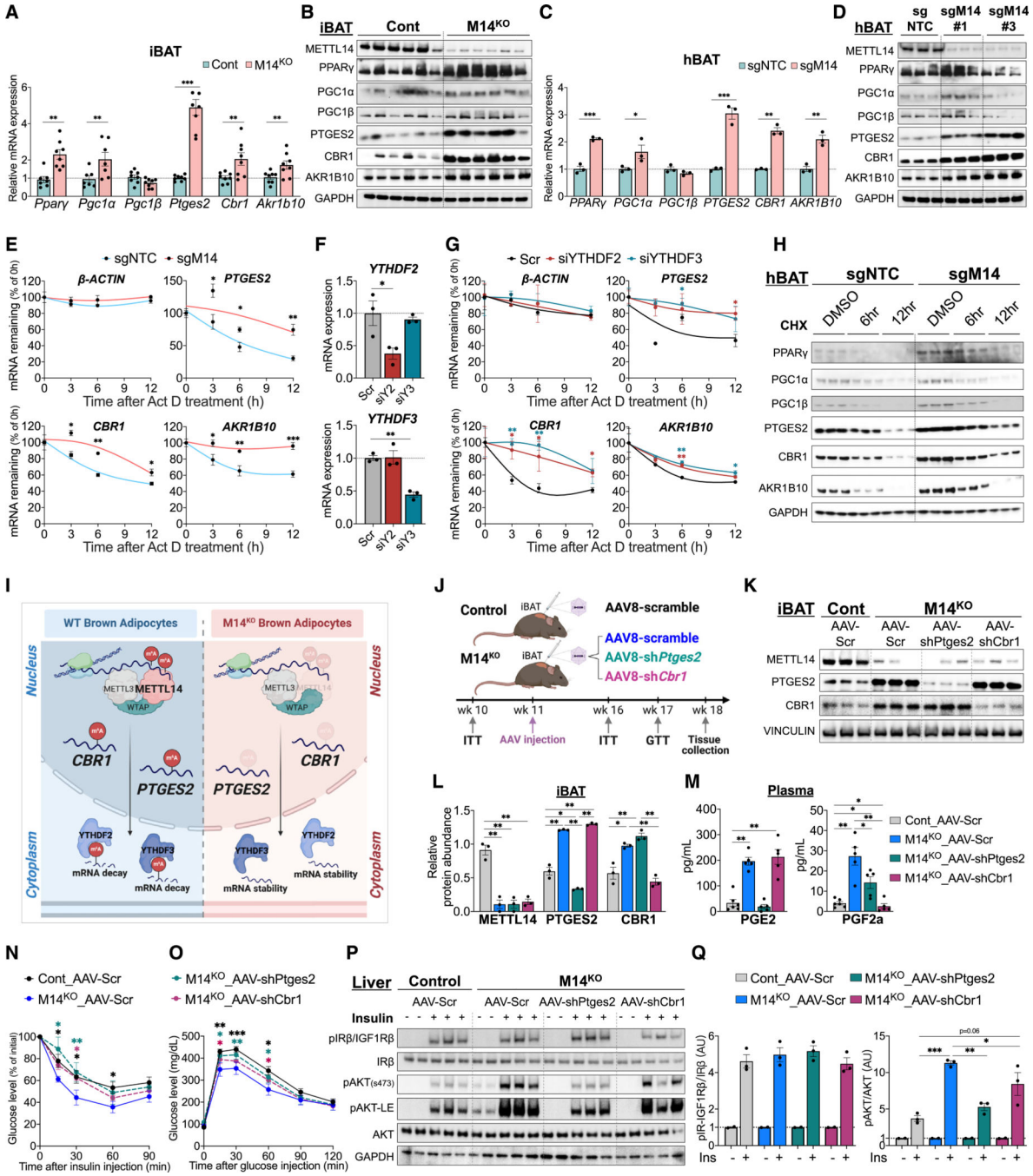

Figure 7. METTL14-mediated m^{6}A installation promotes decay of PGs biosynthesis enzymes and their regulators mRNA in a YTHDF2/3-dependent manner

(A) RT-qPCR analysis of the indicated mRNA expression levels in the iBAT of male control and M14^{KO} mice. mRNA expression levels were normalized to β-actin (n = 7–8/group).

(B) Western blot analysis of the indicated proteins in the iBAT from male control and M14^{KO} mice. GAPDH was used as a loading control (n = 6/group).

(C) RT-qPCR analysis of the indicated mRNAs in sgNTC and sgM14 hBAT cells. mRNA levels were normalized to *ACTB* mRNA (n = 3/group).

(D) Western blot analysis of the indicated proteins in the sgNTC and sgM14 hBAT cells. GAPDH was used as a loading control (n = 3/group).
(E) RT-qPCR analysis of the indicated mRNA expression levels in differentiated sgNTC or sgM14 hBAT cells after a time course treatment with 100 μg/mL actinomycin D (Act D). mRNA levels were normalized to *ACTB* mRNA (n = 3/group).
(F) RT-qPCR analysis of *YTHDF2* and *YTHDF3* mRNAs in differentiated wild-type hBAT cells transfected with siNTC/siYTHDF2/siYTHDF3 siRNA. mRNA levels were normalized to β-*ACTIN* mRNA (n = 3/group).
(G) RT-qPCR analysis of the β-*ACTIN*, *PTGES2*, *CBR1*, and *AKR1B10* mRNA in differentiated wild-type hBAT cells transfected with siNTC/siYTHDF2/siYTHDF3 siRNA and treated with 100 mg/mL Act D for the indicated time. *PTGES2*, *CBR1*, and *AKR1B10* mRNA levels were normalized to β-*ACTIN* (n = 3/group).
(H) Protein stability of indicated proteins in differentiated sgNTC- or sgM14-hBAT cells incubated with 100 μg/mL cycloheximide (CHX) for the indicated time. GAPDH was used as a loading control (n = 3/group).
(I) A proposed model for the molecular mechanism of action that METTL14-mediated m^6A installation destabilizes transcripts encoding prostaglandin biosynthesis enzymes.
(J) Scheme of experimental approach depicting control mice receiving AAV8 eGFP (AAV-scramble), $M14^{KO}$ mice receiving AAV8 eGFP, $M14^{KO}$ mice receiving AAV8 knocking down *Ptges2* (AAV-sh*Ptges2*), and $M14^{KO}$ mice receiving AAV8 knocking down *Cbr1* (AAV-sh*Cbr1*) (n = 5/group).
(K and L) Western blot analysis (K) and quantification (L) of METTL14, PTGES2, and CBR1 in iBAT of the AAV-injected mice.
(M) PGE2 and PGF2a concentrations in mouse plasma measured by ELISAs (n = 6 for cont-AAV-scr; n = 5 for $M14^{KO}$ groups).
(N and O) Intraperitoneal insulin tolerance tests (N) and intraperitoneal glucose tolerance tests (O) of mice injected with AAVs (n = 7 for cont-AAV-scr; n = 5 for $M14^{KO}$ groups).
(P and Q) Western blot analysis (P) and quantification (Q) of pIRβ/IGF1Rβ and $pAKT_{s473}$ in livers of mice 5-weeks post-AAV injections, followed by injection of 1U of insulin via the *vena cava* (n = 2 for non-stimulated groups; n = 3 for insulin-stimulated groups).
All samples in each panel are biologically independent. Data are expressed as means ± SEM. *$p < 0.05$, **$p < 0.01$, and ***$p < 0.001$ by two-tailed unpaired t test (A and C) and two-way ANOVA (E–G, L–O, and Q).
See also Figure S9.

KEY RESOURCES TABLE

REAGENT or RESOURCE	SOURCE	IDENTIFIER
Antibodies		
METTL14 Rabbit	Novus	NBP1–81392; RRID: AB_11021780
α-Tubulin (11H10) Rabbit mAb #2125	Cell Signaling Technology	2125s; RRID: AB_2619646
Rabbit polyclonal anti-p-IGF-I Receptor b (Tyr1131)/Insulin Receptor b (Tyr1146)	Cell Signaling Technology	3021; RRID: AB_331578
Rabbit polyclonal anti-p-IGF-I Receptor b (Tyr1135/1136)/Insulin Receptor b (Tyr1150/1151) (19H7)	Cell Signaling Technology	2969S; RRID: AB_11178660
Insulin Receptor β (4B8) Rabbit mAb	Cell Signaling Technology	3025S; RRID: AB_2280448
Phospho-IGF-I Receptor β (Tyr1135/1136)/ Insulin Receptor β (Tyr1150/1151) (19H7) Rabbit	Cell Signaling Technology	3024L; RRID: AB_331253
Phospho-Akt (Ser473) (D9E) XP Rabbit	Cell Signaling Technology	4060; RRID: AB_2315049
Akt (pan) (11E7) Rabbit mAb #4685S	Cell Signaling Technology	4685S; RRID: AB_2225340
GAPDH (D16H11) XP Rabbit mAb #5174	Cell Signaling Technology	5174S; RRID: AB_10622025
SHIP1 (D1163) Antibody #2728	Cell Signaling Technology	2728S; RRID: AB_2126244
SHIP2 (C76A7) Rabbit mAb #2839	Cell Signaling Technology	2839S; RRID: AB_1031230
SHP-1 (C14H6) Rabbit mAb #3759	Cell Signaling Technology	3759S; RRID: AB_2173694
SHP-2	Cell Signaling Technology	3397T; RRID: AB_2174959
PTP1B Antibody #5311	Cell Signaling Technology	5311S; RRID: AB_10695100
PTEN	Cell Signaling Technology	9188; RRID: AB_2253290
PP2A-B	Cell Signaling Technology	2290; RRID: AB_659890
PP2A-C	Cell Signaling Technology	2259; RRID: AB_561239
PHLPP-1	Proteintech	22789-I-AP; RRID: AB_2750897
PHLPP-2 (PHLPPL)	Proteintech	25244-I-AP; RRID: AB_2879985
PP2B	Cell Signaling Technology	2614s; RRID: AB_2168458
COX-1/Cyclooxygenase-1 Polyclonal antibody	Proteintech	13393–1-AP; RRID: AB_10644323
COX2/Cyclooxygenase 2/PTGS2 Polyclonal antibody	Proteintech	12375–1-AP; RRID: AB_2085127
Recombinant Anti-Prostaglandin E Synthase/MPGES-1 antibody [EPR13765] (ab180589)	Abcam	ab180589; RRID: AB_3492088
C1orf93 Polyclonal antibody	Proteintech	26304–1-AP; RRID: AB_2880471

REAGENT or RESOURCE	SOURCE	IDENTIFIER
AKR1C3 Polyclonal antibody	Proteintech	11194–1-AP; RRID: AB_2224414
Recombinant Anti-Prostaglandin D Synthase (Lipocalin)/PDS antibody [EP12357] (ab182141)	Abcam	ab182141; RRID: AB_2783784
PTGR2 Polyclonal antibody	Proteintech	14164–1-AP; RRID: AB_2173217
Anti-UCP1 antibody (ab155117)	Abcam	ab155117; RRID: AB_2783809
UCP1 (D9D6X) Rabbit mAb #14670	Cell Signaling Technology	14670S; RRID: AB_2687530
METTL3 (D2I6O) Rabbit mAb #96391	Cell Signaling Technology	# 96391S; RRID: AB_2800261
β-Actin (13E5) Rabbit mAb #4970	Cell Signaling Technology	4970S; RRID: AB_2223172
PPAR Gamma Polyclonal antibody	Proteintech	16643–1-AP; RRID: AB_10596794
PGC1a Monoclonal antibody (150ul)	Proteintech	66369–1-Ig; RRID: AB_2828002
Anti-PRDM16 antibody (ab106410)	Abcam	ab106410; RRID: AB_10866455
PTGER3 Polyclonal antibody	Proteintech	24761–1-AP; RRID: AB_2879710
PTGER4 Monoclonal antibody	Proteintech	66921–1-Ig; RRID: AB_2882248
WTAP Polyclonal antibody	Proteintech	10200–1-AP; RRID: AB_2216349
PTGES2 polyclonal antibody	Proteintech	10881–1-AP, RRID: AB_2175066
CBR1 antibody	NOVUS	NBP1–86595, RRID: AB_11038829
Bacterial and virus strains		
LentiCas9-METTL14-FLAG	Generated in the Yi Lab (Joslin Diabetes Center)	N/A
LentiCas9-Empty	Generated in the Yi Lab (Joslin Diabetes Center)	N/A
Edit-R Human All-in-one Set of 3 Lentiviral METTL14 sgRNA, 200μL, 10^7 TU/Ml,QTE-2861014G.1	Dharmacon	VSGH11940–15EG5772157721
Edit-R All-in-one Lentiviral sgRNA mCMV Non-targeting Control #1, 50 mL, 10^7 TU/Ml,QTE-2861014G.1	Dharmacon	VSGC11954
pAAV[shRNA]- EGFP-U6>Scramble_shRNA	VectorBuilder	(Vector ID: VB010000–0023jze)
pAAV[shRNA]- EGFP-U6>mCbr1 [shRNA#1]	VectorBuilder	(Vector ID: VB230907–1315bjg)
pAAV[shRNA]- EGFP-U6>mCbr1 [shRNA#2]	VectorBuilder	(Vector ID: VB230909–1082zrc)
pAAV[shRNA]- EGFP-U6>mCbr1 [shRNA#3]	VectorBuilder	(Vector ID: VB230909–1083apy)
pAAV[shRNA]- EGFP-U6>mPtges2 [shRNA#1]	VectorBuilder	(Vector ID: VB230907–1311mgn)
pAAV[shRNA]- EGFP-U6>mPtges2 [shRNA#2]	VectorBuilder	(Vector ID: VB230909–1080aap)
pAAV[shRNA]- EGFP-U6>mPtges2 [shRNA#3]	VectorBuilder	(Vector ID: VB230909–1081hxn)
Biological samples		

REAGENT or RESOURCE	SOURCE	IDENTIFIER
Human subcutaneous/retroperitoneal/deep abdominal/deep periadrenal/Superficial abdominal/deep perinephric adipose tissues	National Institute of Diabetes and Digestive and Kidney Diseases	N/A
Human plasma samples (Human cohort 1)	Leipzig obesity biobank (Leiria et al.)[9]	N/A
Human plasma samples (Human cohort 2)	Kuopio University Hospital (De Jesus et al.)[35]	N/A
Human plasma samples (Human cohort 3)	Kuopio University Hospital (Halali et al.)[59]	N/A
Horse Serum, New Zealand origin (for myoblast differentiation)	ThermoFisher Scientific	16050130
Chemicals, peptides, and recombinant proteins		
Biotin powder	Sigma-Aldrich	B4639–100MG
D-Pantothenic acid hemicalcium salt	Sigma-Aldrich	P5155–100G
Dexamethasone	Sigma-Aldrich	D1756–25MG
3,3′,5-Triiodo-L-thyronine	Sigma-Aldrich	T2877–100MG
3-Isobutyl-1-methylxanthine	Sigma-Aldrich	I5879–100MG
Indomethacin	Sigma-Aldrich	I7378–5G
Puromycin	American BIO	AB01643–00001
Puromycin dihydrochloride from *Streptomyces alboniger*	SIGMA	P8833–10MG
Polybrene Infection / Transfection Reagent	SIGMA	TR-1003-G
PHOSPHATASE INHIBITOR COCKTAIL2	SIGMA	P5726–1M
PROTEASE INHIBITOR COCKTAIL	SIGMA	P8340–1M
Phosphatase Inhibitor Cocktail 3	SIGMA	P0044–1ML
Lipofectamine RNAiMAX Transfection Reagent	Thermo Fisher Scientific	13778150
RNASE-FREE DNASE KIT	QIAGEN	79254
Glucose Uptake-Glo Assay	Promega	J1342
Rosiglitazone	SIGMA	R2408–10MG
TRIzol Reagent	Thermo Fisher Scientific	15596018
CL316,243	TOCRIS	1499
Insulin (adipocytes differentiation and glucose uptake))	SIGMA	19278
Humaolog (for ITT and Vena Cava injection)	Lilly	ND1048
Krebs-Ringer Solution (Bicarbonate Buffered, without Calcium) - #BSS-255 1L	Boston Bioproducts	#BSS-255
Opti-MEM I Reduced Serum Medium	FISHER	31985062
Prostaglandin F2α (5mg)	CaymanChem	16010
Prostaglandin D2 (5mg)	CaymanChem	12010

REAGENT or RESOURCE	SOURCE	IDENTIFIER
13,14-dihydro-15-keto Prostaglandin E2 (5mg)	CaymanChem	14650
Prostaglandin E2 (5mg)	CaymanChem	14010
Primary Hepatocyte Maintenance Supplements	Primary Hepatocyte Maintenance Supplements	CM4000
Pierce Protein A/G Plus Agarose	Thermofisher	20423
AH 6809 5mg (EP1, EP2, EP3-III, and DP1 antagonist)	Cayman Chemical	14050
AH 23848 5mg (calcium salt) (EP4 antagonist)	Cayman Chemical	19023
ONO-8711 (EP1 antagonist)	Cayman Chemical	14070
AH 6809 (5mg)	Cayman Chemical	14050
Lipofectamine 3000 Transfection Reagent	Thermo Fisher Scientific	L3000008
CAY10598 (1mg) (potent EP4 agonist)	Cayman Chemical	13281
CP 544,326 (1mg) (potent EP2 agonist)	Cayman Chemical	22945
17-phenyl trinor Prostaglandin E2 (1mg) (potent EP1 and EP3 agonist)	Cayman Chemical	14810
L-826,266 (1mg) (EP3 antagonist)	Cayman Chemical	18538
PF-04418948 (EP2 antagonist)	Cayman Chemical	15016
Ebopiprant (Synonyms: OBE022)-5mg	MedChemExpress	2005486–31-5
Forskolin (25mg)	Sigma	F3917–25MG
Normal Saline, 500mL	Thomas Scientific	786–560
Mouse IgG1 Isotype Control Antibody	Creative Biolabs	MOB-065CQ-LowE
Anti-Human PGE2 Recombinant Antibody (2B5)	Creative Biolabs	TAB-1022CL-LowE
Critical commercial assays		
RNase-Free DNase Set (250)	QIAGEN	79256
Insulin Mouse Ultra Sensitive ELISA	Crystal Chem	90082
Prostaglandin E2 Express ELISA Kit (96 strip)	Cayman Chemical	500141
Prostaglandin F2α ELISA Kit (96 strip)	Cayman Chemical	516011
Magnetic mRNA Isolation Kit	NEB	S1550S
Triglyceride-Glo Assay	Promega	J3160
Free Fatty Acid Assay Kit - Quantification	Abcam	ab65341
Deposited data		

REAGENT or RESOURCE	SOURCE	IDENTIFIER
m^{6}A-sequencing and RNA-sequencing data in mouse brown adipose tissue and differentiated human brown adipocytes	GSE23249	https://www.ncbi.nlm.nih.gov/geo/query/acc.cgi?acc=GSE232491
Source data	N/A	Data S1 - Source Data
Experimental models: Cell lines		
hBA A41	Immortalized by the Tseng Lab (Joslin Diabetes Center)	(Xue et al.[60])
hWA A41	Immortalized by the Tseng Lab (Joslin Diabetes Center)	(Xue et al.[60])
C2C12	ATCC	Cat# CRL-1772
HepG2	ATCC	HB-8065
GIBCO Human Skeletal Myoblasts	ThermoFisher Scientific	A11440
Human Plateable Hepatocytes, 5-Donor	ThermoFisher Scientific	HMCPP5
Experimental models: Organisms/strains		
C57BL/6J DIO	The Jackson Laboratory	RRID: IMSR_JAX:38 0050
BKS.Cg-Dock7m +/+ Leprdb/J	The Jackson Laboratory	RRID: IMSR_JAX:00 0642
LIRKO mice	Michael et al.[21]	N/A
Hemizygous for Tg(Ucp1-cre)1Evdr	The Jackson Laboratory	Cat# 024670
Mettl14-flox	Developed in the He Lab (University of Chicago)	N/A
Oligonucleotides		
Primers for qPCR	See Table S1 – this paper	N/A
ON-TARGETplus Human YTHDF1 siRNA (SMARTPool)	Dharmacon	L-018095–02-0005
ON-TARGETplus Human YTHDF2 siRNA (SMARTPool)	Dharmacon	L-021009–02-0005
ON-TARGETplus Human YTHDF3 siRNA (SMARTPool)	Dharmacon	L-017080–01-0005
ON-TARGETplus Non-targeting Control Pool	Dharmacon	D-001810–10-05
Software and algorithms		
GraphPad Prism	GraphPad Software, San Diego, CA	Version 8
ImageJ	NIH	N/A
BioRender	N/A	https://biorender.com/

REAGENT or RESOURCE	SOURCE	IDENTIFIER
Other		
Physitemp TH-5 Thermalert Clinical Montoring Thermometer	FISHER	NC0883824
Physitemp RET-3 Rectal Probe for Mice	FISHER	NC9713069